Cement and Concrete Research 181 (2024) 107527

Contents lists available at ScienceDirect

Cement and Concrete Research

journal homepage: www.elsevier.com/locate/cemconres

Sodium aluminate activated waste glass: Reduced efflorescence behavior by C(N)−A−S−H transformation

Tao Liu [a,b,c], Yuxuan Chen [a], Bo Yuan [d], Weitan Zhuang [a], H.J.H. Brouwers [c,d], Qingliang Yu [a,c,*]

[a] School of Civil Engineering, Wuhan University, 430072 Wuhan, PR China
[b] DTU sustain, Department of Environmental and Resource Engineering, Technical University of Denmark, 2800 Kgs Lyngby, Denmark
[c] Department of the Built Environment, Eindhoven University of Technology, 5600MB Eindhoven, the Netherlands
[d] State Key Laboratory of Silicate Materials for Architectures, Wuhan University of Technology, 430070 Wuhan, PR China

ARTICLE INFO

Keywords:
Waste glass
$NaAlO_2$ activation
NMR
C(N) − A − S − H
Efflorescence

ABSTRACT

Waste glass has been highly used in alkali activated materials, but the efflorescence behavior remains an intractable issue. This study investigates the effect of sodium aluminate as an activator to activate waste glass with the aim to mitigate the efflorescence behavior, and blast furnace slag is used as calcium source as well as to promote the early age strength. The gel structure (reaction product) was characterized by ^{29}Si and ^{27}Al NMR, subsequently the efflorescence behavior was investigated. Results show that sodium aluminate provides more $Al(OH)_4^-$, which acts as cross-linking agents, linking silicate tetrahedra to form a three-dimensional gel network. A longer mean chain length of gels increases hydrogen sites at end-chain Q^1 silicate species, which can be replaced by cations along the silicate chain. The promoted formation of C(N)−A−S−H gel captures more Na^+ in the pore solution, contributing to a limited Na^+ leaching and higher resistance towards efflorescence.

1. Introduction

Waste glass (WG) is a typical inorganic solid waste material derived from both daily life and industrial production [1,2]. Currently, the utilization of waste glasses for the manufacture of alkali activated materials (AAMs) has been confirmed, which might increase the recycling or reuse potential [3–5]. The suitability of using waste glass to replace common precursors such as fly ash and slag has been clarified [6,7]. The durability performance of resulting AAMs with waste glasses is affected by different parameters, which have not yet been evaluated systematically [8]. For instance, the efflorescence of alkali activated waste glass (AAWG) becomes an intractable problem, particularly when the materials are exposed to a humid environment due to the high concentration of free alkalis in AAWG [9,10].

Efflorescence has long been a challenging topic of investigation. Capillary motion causes the pore solution to move through the concrete matrix and evaporate from its surface, leaving the deposit of free alkali cations on the surface. The leached alkali cations react with atmospheric CO_2, causing the formation of white carbonate surface deposits known as efflorescence [11]. The efflorescence causes aesthetic degradation, damage to the surface of the material, and reduced durability [12]. The accumulation of salts can lead to material deterioration, including spalling and cracking [13]. These problems can compromise the structural integrity of buildings or structures, and in severe cases, may require costly repairs or even reconstruction. Efflorescence also ruins the perception of color and the appreciation of concrete buildings [14]. Cyr et al. [15] reported that the high dosage of alkalis and low content of aluminum in glass cullet was the main reason for the high extent of efflorescence. The main hydration products of AAWG are mostly Si-high, Al- and Ca-low gels [7]. The hydrolytic stability of silicate gels in AAWG is poor, and it is attributed to easy depolymerization of the Si-high, Al- and Ca-low gels caused by the removal of physically bound water under long-time curing or high-temperature environment [16]. Consequently, AAWG is weak to prevent the occurrence of efflorescence. To improve the resistance of efflorescence, Al-rich and Ca-rich materials, e.g. slag, were applied in the AAWG matrix to enhance the stability of Si-rich gels [11]. Vafaei et al. [17] attempted to use reactive alumina by incorporating calcium aluminate cement to modify the waste glass geopolymer. The formation of sodium aluminosilicate hydrates (N−A−S−H) resulted in improved resistance towards efflorescence. However, excessive sodium oxide remaining unreacted in the precursor materials and activator could particularly suffer unsightly efflorescence caused by mobile alkalis [18]. Relatively weak binding of Na in the geopolymer structure results in the tendency of efflorescence. This is because Na^+ is easy to

* Corresponding author at: School of Civil Engineering, Wuhan University, 430072 Wuhan, PR China.

https://doi.org/10.1016/j.cemconres.2024.107527
Received 27 November 2023; Received in revised form 7 March 2024; Accepted 28 April 2024

move within the pore solution and penetrates to the surface of the matrix. Therefore, it is hypothesized that enhancing the participation of Na in the formation of C(N)−A−S−H gels can be a feasible way to enhance the efflorescence resistance of AAWG, as less free Na^+ is available to move to the surface of the matrix in the humid environment.

To discuss it further, the formation of C(N)−A−S−H influences the evolution of microstructure, which affects the resistance of efflorescence and the mechanical property. The changes in Al/Si and Al/Na ratios play important roles in the generation of reaction products. In AAMs matrix, Al—O tetrahedra (denoted as $Al(OH)_4^-$) are rich in the pore solution at the beginning of reaction process. Because Al—O bond is weaker than the Si—O bond dissolving from raw materials [19]. A high Al/Si ratio promotes a high degree of Al-O-Si bond. More Si—O tetrahedra (denoted as $Si(OH)_4$) are able to involve into the C(N)−A−S−H chain. Therefore, A higher Al/Si ratio can promote the C(N)−A−S−H formation in the matrix. Besides, the higher Al/Na ratio in the system increases the Si—Al chain interacting with Na to form C(N)−A−S−H in the geopolymer products [20]. Therefore, the availability of $Al(OH)_4^-$ plays an important role in the formation of C(N)−A−S−H gels. Our previous study has revealed that sodium aluminate activator could provide extra $Al(OH)_4^-$ that promotes the C(N)−A−S−H formation in the activated slag matrix [21–23]. The sodium aluminate can potentially supplement Al resource in the waste glass matrix, promoting the C(N)−A−S−H formation. The utilization of sodium aluminate activator changes the Al/Si and Al/Na ratios, which influences the C(N)−A−S−H formation significantly in the matrix. The incorporation of $Al(OH)_4^-$ into a silicate chain could lead to the remarkable transformation of the gel structure [24]. To date, no literature has reported the property of sodium aluminate activated waste glass (SAAG). The formed gel structure influenced by the sodium aluminate activator remains unknown areas. It is urgent to investigate its mechanism in terms of sodium aluminate activated waste glass.

The objective of this study is to investigate the efflorescence of alkali activated waste glass. Sodium aluminate was used to as the activator to activate the precursors in order to evaluate the effect of extra $Al(OH)_4^-$ on gel structure transformation and explore its impact on efflorescence mitigation. A small amount of blast furnace slag was used to promote the early age strength development, as well as to provide additional calcium. Sodium hydroxides and their hybrid activator were used as the control group. The reaction products of sodium aluminate activated slag and waste glass (SAASG) were determined by Quantitative X-ray diffraction (QXRD), thermogravimetry (TG), and Four-transform inferred spectroscopy (FTIR). The gel structure was characterized by nuclear magnetic resonance (NMR). The microstructure was assessed by Scanning electron microscopy (SEM). Moreover, the efflorescence behavior and compressive strength of paste samples were evaluated. The effect of extra $Al(OH)_4^-$ on the main chain length and composition of gels was

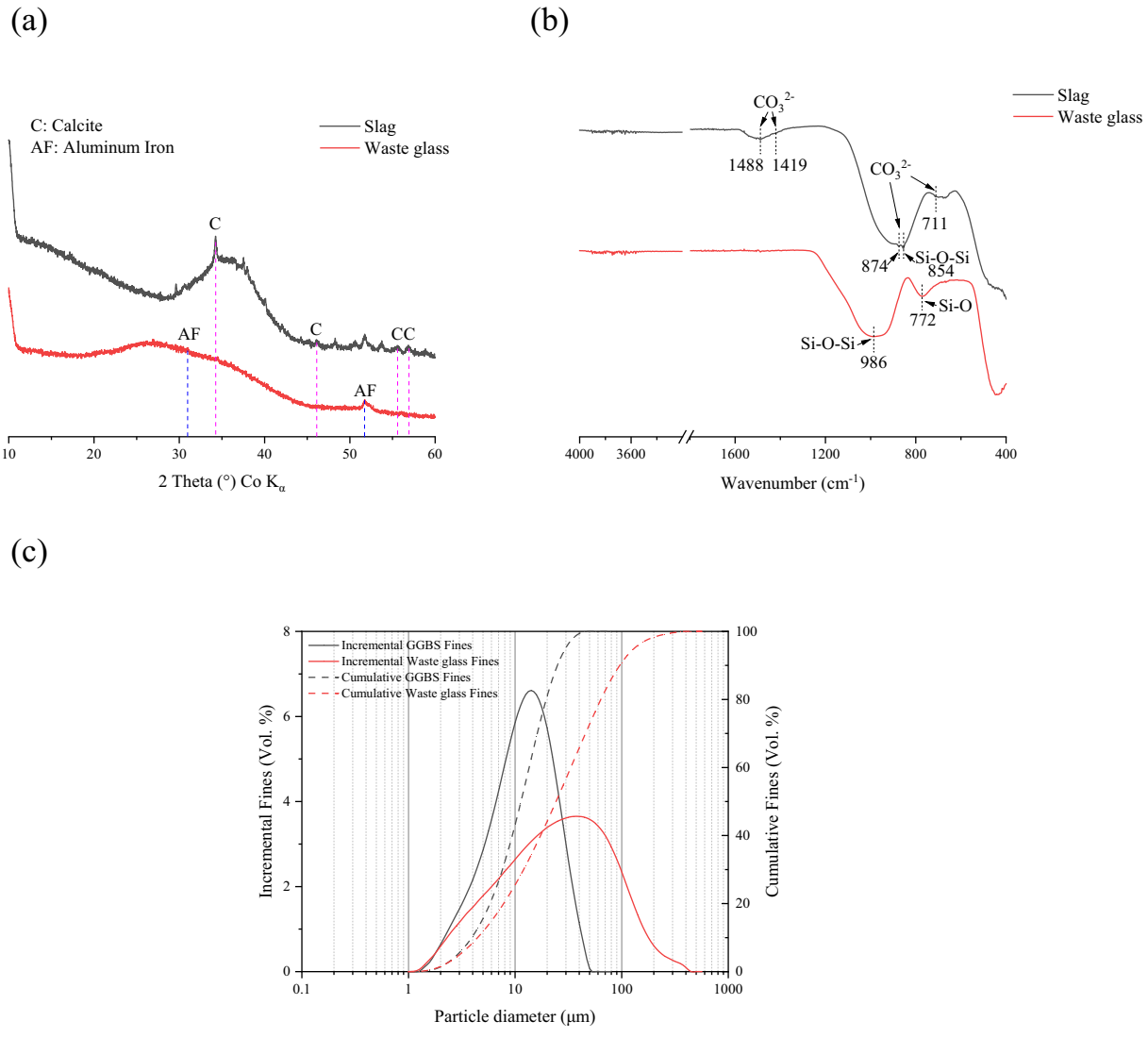

Fig. 1. Properties of slag and waste glass: (a) XRD; (b) FTIR; (c) PSD.

studied. Further, the mechanism of efflorescence behavior was proposed to provide insight into stabilizing Na^+ leaching by crosslinked C(N)–A–S–H formation.

2. Methodology

2.1. Materials

The ground granulated blast-furnace slag and waste glass (provided by Maltha, The Netherlands) were utilized in this study. The received waste glass pellet was ground by a disk mill for 5 min to achieve the desired particle size. Fig. 1(a) shows that the slag and waste glass are mainly composed of amorphous phases. The slag contains a small amount of calcite and the waste glass contains a small amount of aluminum iron. Fig. 1(b) shows the FTIR analysis of the processed waste glass and slag. The stretching of Si-O-Si can be observed at 986 cm^{-1} in waste glass. It also indicates the stretching of carbonate in slag at 1488 and 1419 cm^{-1}. The laser particle size analyzer (Mastersizer 2000, Malvern Instruments, UK) was used to determine the particle size distribution (PSD) of raw materials (as shown in Fig. 1(c)). The median particle size (d_{50}) of slag and waste glass powder were 12.743 and 27.194 μm, respectively. X-ray fluorescence spectrometry (XRF, PANalytical Epsilon 3) was used to examine the chemical composition of slag and waste glass powder (as shown in Table 1). The specific density, specific surface area, and loss on ignition of slag and waste glass were also determined and shown in Table 1.

2.2. Mix design

The slag and waste glass were mixed in a 1:9 (slag: waste glass) mass ratio as the solid precursor, which was activated by sodium hydroxide (NH), sodium aluminate (NA), and their hybrid (NHNA) solutions. Simultaneously, the equivalent Na_2O contents vary from 3 to 5 wt% (see the sample IDs in Table 2). Each SAASG blend was stirred for 10 min during the mixing to realize the uniformity of the pastes. The fresh SAASG pastes were poured into the plastic cubic molds with a dimension of 4 cm × 4 cm × 4 cm and then sealed by plastic membranes. In the first stage, all the samples were cured at room temperature (20 °C). After 24 h, the samples were cured at 75 °C for 24 h. The samples remain sealed during the thermal curing process to prevent moisture loss. Then, after thermal curing for 24 h, all the samples were demoled and continued to cure in the laboratory environment (open-air curing) in the room with stable temperature (20 °C) and 60 % humidity.

The activators used in this study were sodium hydroxide, sodium aluminate, and their mixture (hybrid activator). Analytical grade sodium-hydroxide pellets and sodium aluminate pellets were dissolved in deionized water (separately or together) to prepare activators 6 h before application. The hybrid activator of sodium hydroxide and sodium aluminate was in different aluminate modulus (Al_2O_3/Na_2O) from 0 to 1.

Table 1
Chemical composition (wt%), specific density, specific surface area, and loss on ignition of slag and waste glass.

Chemical composition	GGBS (wt%)	Waste glass (wt%)
Na_2OH	/	10.24
MgO	8.64	1.09
Al_2O_3	13.32	1.83
SiO_2	29.65	71.27
SO_3	2.66	/
K_2O	/	0.77
CaO	43.01	13.62
TiO_2	1.50	/
Fe_2O_3	/	0.64
Cl	0.01	0.10
Others	1.20	0.45
LOI* (1000 °C)	−0.91	0.28
Specific density (g/cm^3)	2.78	2.44
Specific surface area (m^2/g)	1.67	0.61

2.3. Test methods

2.3.1. Quantitative X-ray diffraction

X-ray diffraction (XRD) was performed using a Bruker D4 Phaser instrument emitting Co-K_α radiation (40 kV, 30 mA). The crushed, powdered SAASG pastes were measured with a step size of 0.05° and a counting time of 1 s/step. The 2θ range was 10–90°. For the quantitative X-ray diffraction (QXRD) study, all the pastes were ground by ball milling at level 3 speed for 15 min before the test. The silicon powder (10 wt%, Siltronix, France) was added as an internal standard to the paste samples. For the quantification of mineral phases in the samples, Rietveld analysis was performed using TOPAS software (version 4.2, Bruker). Before the test, the paste samples were ground into powder, immersed in 2-propanol for 24 h to stop the hydration process, and then dried to constant mass at 60 °C for 3 d.

2.3.2. Thermogravimetry

Thermogravimetry (TG) tests were performed on ≈100 mg crushed, powdered paste samples by using an STA 449 F1 instrument at a heating rate of 10 °C/min. Notably, the aluminum crucible lid had to be used in case the expansion of the waste glass powder under the thermal process. Experiments were carried out from 40 °C to 1000 °C, in which N_2 was used as the carrier gas. The same hydration stoppage treatment was performed before the test as well.

2.3.3. Fourier-transform infrared spectroscopy

Fourier-transform infrared spectroscopy (FTIR) analysis was performed using a Varian 670-IR spectrometer with a wavelength range of 400 to 4000 cm^{-1} with a resolution of 1 cm^{-1}. The powdered samples were prepared following the same procedure as discussed above after hydration stoppage treatment.

2.3.4. Nuclear magnetic resonance

The solid-state magic angle spinning nuclear magnetic resonance (MAS NMR) (JNM-ECZ600R) measurements were carried out at a 14.01 T magnet and a resonance frequency of 99 MHz for ^{29}Si and 132 MHz for ^{27}Al. The ^{29}Si MAS NMR spectra were recorded using a 4 mm CPMAS probe head and a 4 mm zirconia rotor by employing a spinning speed of 12 kHz, a 4 μs excitation pulse, and a 20 s relaxation delay. The solid-state ^{27}Al MAS NMR spectra were recorded using a 2.5 mm CPMAS probe head and a 2.5 mm zirconia rotor spinning at a speed of 12 kHz, a 1 μs excitation pulse, and a 0.5 s relaxation delay.

The deconvolution of the 29Si MAS NMR spectra was carried out using Origin 2022. The multipeak fit was used to calculate the area of each peak of silicon and aluminum state that exists in the spectra with Gaussian function according to the literature [25,26]. The cumulative integrated percentage of each silicon and aluminum in SAASG was obtained to calculate the mean chain length (MCL) and Al—Si substitution of C(N)–A–S–H [27].

^{29}Si MAS NMR has revealed important information regarding C(N)–A–S–H formation in the hydrated matrix. Resonances from the Q^1, Q^2, and $Q^2(1Al)$ sites, which constitute the silicate chains in the C(N)–A–S–H gel, have been seen using ^{29}Si MAS NMR [28,29]. The mean chain length (MCL) of non-crosslinked C(N)–A–S–H gel can be calculated by using Eq. (1), while the MCL of crosslinked C(N)–A–S–H gel can be calculated by using Eq. (2). The Al—Si substitution in the tetrahedral chains can be obtained from the intensities of the Q^1, Q^2, and $Q^2(1Al)$ resonances (Eq. (3)), as reported by Richardson et al. [30,31].

$$MCL_{nc} = \frac{2\left[Q^1 + Q^2 + \frac{3}{2}Q^2(1Al)\right]}{Q^1} \quad (1)$$

Table 2
Mix design of paste samples.

Sample	w/b[a]	$NaAlO_2$(g)	NaOH(g)	Na_2O (wt%)	Al_2O_3/Na_2O (In activator)	Glass powder (g)	Slag(g)
NA3	0.4	7.935	/	3	1	90	10
NA4	0.4	10.581	/	4	1	90	10
NA5	0.4	13.225	/	5	1	90	10
NHNA3	0.4	3.968	1.935	3	0.5	90	10
NHNA4	0.4	5.291	2.580	4	0.5	90	10
NHNA5	0.4	6.613	3.225	5	0.5	90	10
NH3	0.4	/	3.871	3	0	90	10
NH4	0.4	/	5.161	4	0	90	10
NH5	0.4	/	6.452	5	0	90	10

[a] w/b = water to binder ratio in mass

$$MCL_c = \frac{4\left[Q^1 + Q^2 + Q^2(1Al) + Q^3 + 2Q^3(1Al)\right]}{Q^1} \quad (2)$$

$$\frac{Al[IV]}{Si} = \frac{\frac{1}{2}Q^2(1Al)}{Q^1 + Q^2 + Q^2(1Al)} \quad (3)$$

2.3.5. Scanning electron microscopy / energy dispersive spectroscopy

After the compressive strength tests of samples at 3 and 28 days, the fragments of each paste sample were collected. The microstructure of the selected samples was examined by scanning electron microscopy (SEM). The composition of the gels was determined by an energy dispersive spectroscopy (EDS) instrument based on the SEM graphs. The clusters of Si-Al-Ca-Na were normalized to obtain the quaternary phase (Si-Al-Ca-Na) diagrams. Then the composition of C(N)−A−S−H can be examined.

2.3.6. Efflorescence testing

2.3.6.1. Visual efflorescence testing. To qualitatively investigate the efflorescence behavior, the 3-day cured Ø2cm × 5 cm cylinder pastes were placed in transparent plastic petri dishes. The petri dishes were filled with deionized water every day to keep the immersion of samples 1 cm in height. The deionized water could accelerate the leaching of Na^+ aggravating the efflorescence behavior. The evolution of visual efflorescence was recorded on a time scale. The results of the visual efflorescence test were obtained qualitatively by visual comparison of the samples.

2.3.6.2. Indicative efflorescence testing. To evaluate the efflorescence degree of each sample, the experiment was performed with a indicative leaching test. The crushed fragments of all the geopolymer paste at 28 days and 56 days of open-air curing were collected after passing a No. 200 sieve to minimize the influence of particle size. 1.00 g of each geopolymer powder was added to 100 ml of deionized water. The solutions were stirred for 30 min and kept at ambient temperature for 24 h to allow the leaching of free Na^+, Ca^{2+}, and Mg^{2+} (major leachable alkali ions) from the geopolymer paste [11]. Then the leachates were placed in the oven after the filtration to allow the evaporation of water. The mass of dissoluble salts was measured to evaluate the extent of efflorescence following Eq. (4):

$$E(wt.\%) = \frac{m_d}{1\ g\ (geopolymer\ powder)} \times 100\% \quad (4)$$

where E(wt.%) is the extent of efflorescence; m_d is the mass of dissoluble salts in 1 g of geopolymer powder.

2.3.7. Compressive strength

After 3- and 28-day air curing, all the cubic SAASG pastes were tested for compressive strength by a constant loading rate of 2400 N/s until the fracture load. The strength value of each mix was recorded by the average of 3 samples.

3. Results

3.1. Reaction products

3.1.1. Quantitative X-ray diffraction

Fig. 2 illustrates the XRD patterns and their quantitative analysis of AASG at 3 and 28 days. There is a large difference in crystalline phase assemblages between sodium aluminate (mainly zeolite A), sodium hydroxide (mainly natrite), and hybrid activator (mainly zeolite Na—P_1) activated slag and waste glass either at 3 or 28 days. It is interesting that katoite is only observed in the samples with $NaAlO_2$ participation, which is attributed to the provided $Al(OH)_4^-$ from $NaAlO_2$. Hydrotalcite is only observed in the samples with NaOH participation.

For sodium aluminate activated slag and waste glass (NA samples), there is a significant increase of zeolite A (ICDD00-039-0222, $Na_{96}Al_{96}Si_{96}O_{384}{\cdot}216H_2O$) from 3 to 28 days. It is associated with the extra $Al(OH)_4^-$ (from $NaAlO_2$ activator) that promotes the zeolite formation [21]. No zeolite Na—P_1 (ICDD:00-039-0219, $Na_6Al_6Si_{10}O_{32}{\cdot}12H_2O$) is present at 3 days but it appears at 28 days in NA4 and NA5 samples with a limited amount. It is due to the higher alkalinity of the NA4 and NA5. A higher pH environment leads to enhanced dissolution of silicate monomers in the pore solution, which favors the formation of zeolite Na—P_1 that needs more silicate than zeolite A. Meanwhile, the zeolite Na—P_1 is more thermodynamically stable than zeolite A at a longer reaction time [32,33]. The Si/Al ratio of precursors and activators plays important roles in the type of zeolite formation [34–36]. A high possibility is that the higher Si content in waste glass may transfer zeolite A to zeolite Na—P_1 because zeolite A needs more Al resources while zeolite Na—P_1 needs more Si resources. Another zeolite (ICDD: 00–031-1271, $1.08Na_2O{\cdot}Al_2O_3{\cdot}1.68SiO_2{\cdot}1.8H_2O$) is produced in NA4 and NA5 with a small amount but absent in NA3. Those zeolite phases are normally formed with calcium sodium aluminosilicate hydrates (C(N)−A−S−H) together in the $NaAlO_2$ activation system [21]. The presence of katoite (ICDD: 01–077-1713, $Ca_{2.93}Al_{1.97}(Si_{.64}O_{2.56})(OH)_{9.44}$) in NA samples is due to the participation of slag from the precursors. The dissolved Ca^{2+} from slag reacts with $Al(OH)_4^-$, leading to the formation of katoite. Moreover, the elevated alkalinity (NA3 to NA5) promotes the dissolution of Ca^{2+}, resulting in a higher katoite formation.

For sodium hydroxides activated slag and waste glass (NH samples), the natrite (ICDD: 00–037-0451 Na_2CO_3) formation increases with the increased alkalinity from NH3 to NH5, which is also the primary crystalline phase. The presence of calcite (ICDD: 01–086-2341, $CaCO_3$) and hydrotalcite (ICDD: 00–014-0191, $Mg_6Al_2CO_3(OH)_{16}{\cdot}4H_2O$) are attributed to the dissolution of Ca^{2+} and Mg^{2+} from slag. They also increase with the elevated equivalent Na_2O content. The calcite is generated by carbonation of the samples during air curing. In the meantime, no magnesite (ICDD: 01–086-2348 $MgCO_3$) is detected at 3 days but it is

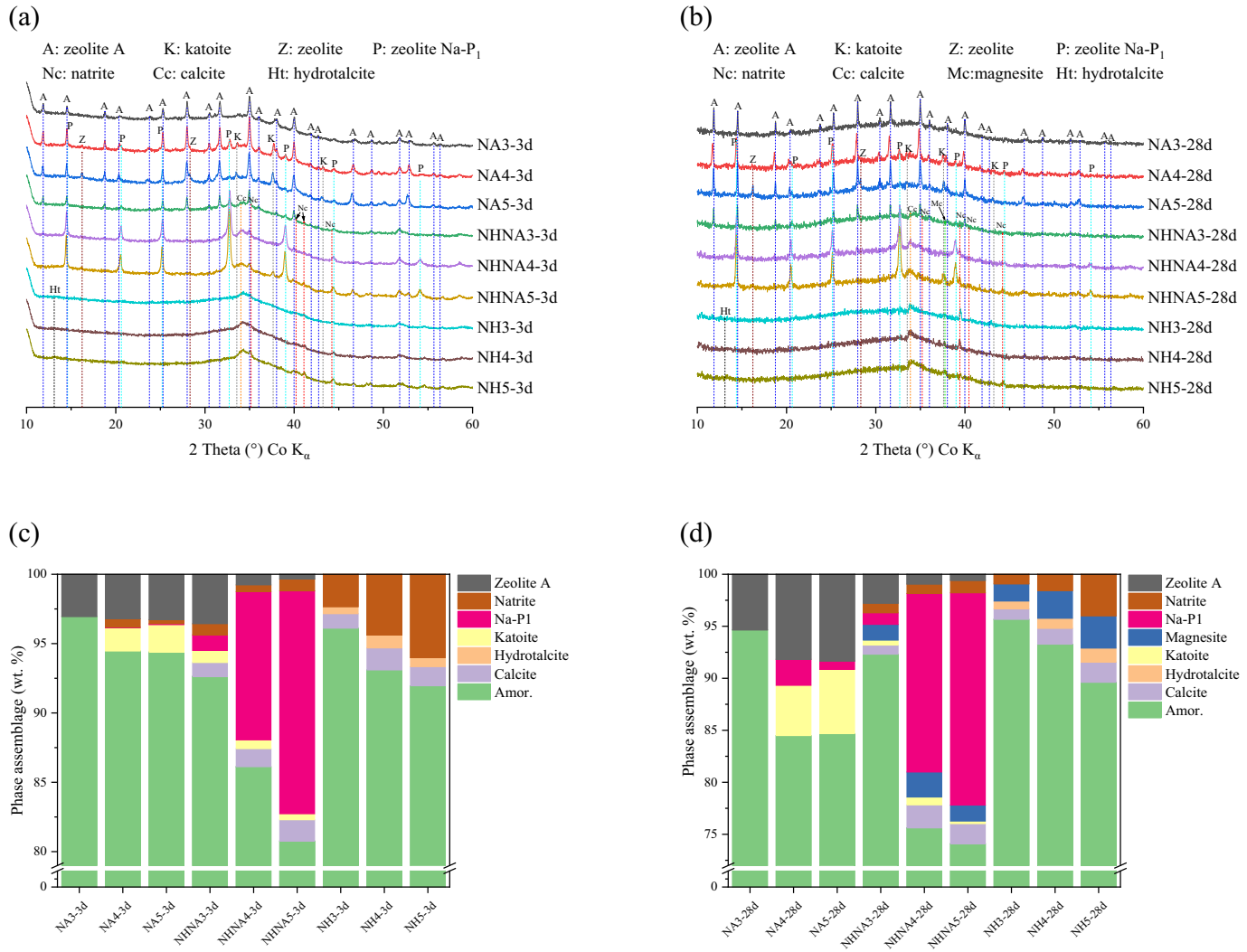

Fig. 2. SAASG pastes XRD at (a) 3 days; (b) 28 days; QXRD at (c) 3 days; (d) 28 days.

observed at 28 days. The formation of hydrotalcite mainly consumes the dissolved Mg^{2+} at the early reaction process, so no magnesite is formed at 3 days. Along with the air curing, more available Mg^{2+} from slag reacts with CO_2, resulting in the formation of magnesite at the late stage.

For hybrid activator activated slag and waste glass (NHNA samples), there is a large amount of zeolite Na—P_1 (ICDD: 00–039-0219, $Na_6Al_6Si_{10}O_{32}{\cdot}12H_2O$) generation from 3 to 28 days. However, NHNA3 shows that zeolite A is the primary crystalline phase, which is different from

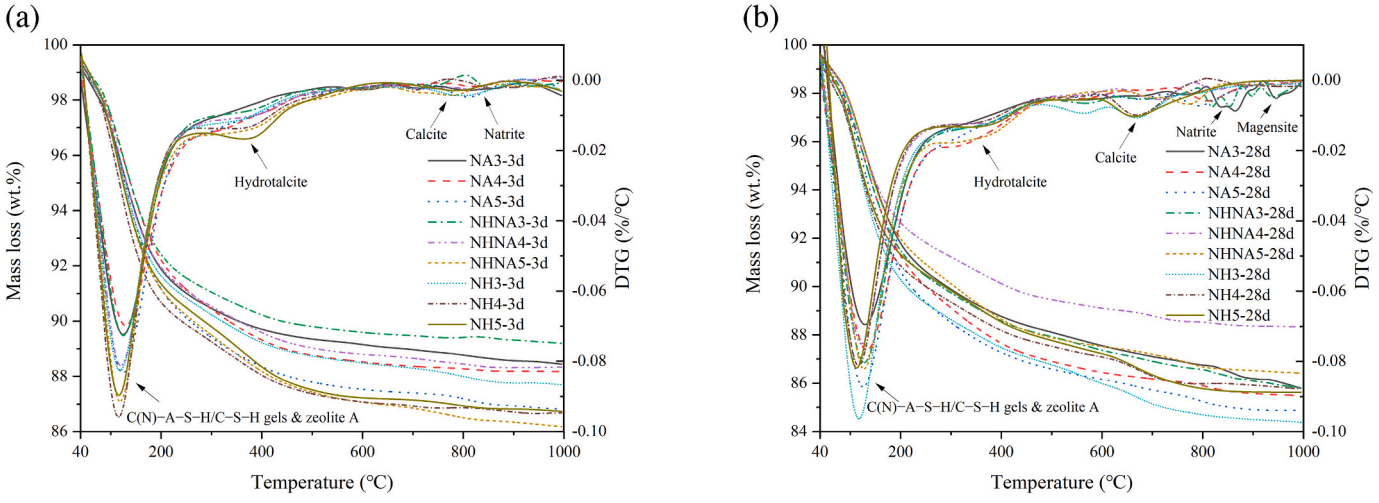

Fig. 3. TG and DTG of SAASG at (a) 3 days; (b) 28 days.

NHNA4 and NHNA5. The alkaline pH environment facilitates the transformation of zeolite A into zeolite Na—P_1, owing to the higher concentration of silicate monomers present in the pore solution, as previously presented. In the meantime, the elevated pH environment is more vulnerable to carbonation. It results in the increase of calcite and magnesite generation from 3 to 28 days by comparing NHNA3 ~ NHNA5.

Overall, the primary reaction products of the NA and NHNA sample are zeolite and C(N)−A−S−H gels. However, the products of NH samples are sodium/magnesium carbonate and Si-high, Al- and Ca-low gel under air curing conditions.

To ascertain whether the formation of Natrite is a result of carbonation or in-situ formation, GEMS modeling was conducted for the NaOH and $NaAlO_2$ activated waste glass/slag system (in Supplementary materials). The results (shown in Fig. SP1) demonstrate that open-air curing process is the reason for the formation of carbonated phases (natrite, calcite, and magnesite).

3.1.2. Thermogravimetry

The thermogravimetry (TG) and differential thermograms (DTG) curves of the SAASG pastes, as a function of different curing ages, are presented in Fig. 3. The detailed information is summarized in Table 3 and Table 4. For 3-day curing pastes (Fig. 3(a)), the first large peak of DTG of NA samples is due to the loss of moisture water (40–100 °C) [2], decomposition of C(N)−A−S−H (100–300 °C) [21], and the zeolite A (40–200 °C) [37]. As can be seen, the mass losses of this temperature range increase with the elevated equivalent Na_2O content, namely the mass losses of NA3 ~ 5 are 9.54, 9.56, and 10.59 wt%, respectively. The difference is mainly from the decomposition of C(N)−A−S−H, because the zeolite A contents in NA pastes are similar to each other as mentioned in QXRD results. The reason is that a higher $NaAlO_2$ in the matrix provides more Al—O tetrahedra in the pore solution, which promotes the formation of C(N)−A−S−H gels [21]. For NHNA samples at 3 days, the largest decomposition peak in DTG is derived by the loss of moisture water (40–100 °C) [2], decomposition of C(N)−A−S−H (100–300 °C) [21], the zeolite A (40–200 °C) [37], and zeolite Na—P_1 (25–400 °C) [38]. It is quite similar to NA samples at 3 days. Because these hydrated phases are promoted by the $NaAlO_2$ activator. However, the NaOH participation results in the reduction of zeolite A formation but an increase of zeolite Na—P_1. Thus, the primary mass losses (first decomposition peak) in NHNA4 and NHNA5 samples are from zeolite Na—P_1. It is in good agreement with the QXRD results. Interestingly, the decomposition of calcite ($CaCO_3$) at around 700 °C [39] and natrite (Na_2CO_3) at around 850 °C [40] are observed. This is attributed to the NaOH activator that increases the alkalinity of the samples. It leads to the samples being vulnerable to carbonation. For NH samples at 3 days, the largest peak of DTG is mainly associated with the loss of moisture water (40–100 °C) [2], decomposition of C−(A)−S−H gels, and the first decomposition peak of hydrotalcite (150–250 °C) [41]. At the same time, the second decomposition peak of hydrotalcite is shown at around 400 °C as well [41]. These are typical hydrated phases from NaOH activated slag [42]. The elevated alkalinity of NH samples also leads to slightly higher amount of hydrotalcite formation. It is owing to more dissolved Mg^{2+} and $Al(OH)_4^-$ from slag to form more hydrotalcite. Besides, a small amount of calcite decomposes at around 700 °C in NH samples [39]. At the same time, a small amount of natrite decomposes at around 850 °C [40]. Those carbonated phases, confirmed by QXRD analysis, are originated from the carbonation during the air-curing.

Fig. 3(b) exhibits TG and DTG curves at 28 days, the NA3 ~ 5 samples show 10.11, 10.89, and 11.50 wt% mass losses (40–300 °C), respectively. The mass losses, like 3-day NA samples, include the loss of moisture water, decomposition of C(N)−A−S−H, zeolite A, and a small amount of zeolite Na—P_1. Compared to 3-day NA pastes, the increase in mass losses is associated with the elevated formation of C(N)−A−S−H and zeolite A. For 28-day NHNA pastes, there is a large amount of C(N)−A−S−H and zeolite Na—P_1 decomposition, as well as a small amount of zeolite A decomposition before 300 °C. It is similar to 3-day NHNA pastes. However, the decomposed peaks of calcite and magnesite can be observed at around 700 and 900 °C, respectively. It is related to the carbonation of NHNA samples. Besides, the largest decomposed peak of 28-day NH pastes is linked with C−(A)−S−H gels. Furthermore, the remarkable decomposition of calcite and natrite can be obtained at 700 and 850 °C. It is also associated with the severe carbonation of NH samples.

Particularly, comparing the NA, NHNA, and NH samples, the carbonated phases (calcite, natrite, and magnesite) decrease with aluminate modulus regardless of curing ages. The aluminate contributes to the formation of Al-rich zeolite and C(N)−A−S−H gels, resulting in the less available Na^+, and Ca^{2+} to form natrite and calcite. It can be concluded that the aluminate modulus increases the capacity of carbonation resistance.

3.1.3. Fourier-transform infrared spectroscopy

Fig. 4 illustrates the FTIR spectra of SAASG pastes at 3 and 28 days. As can be seen from Fig. 4 (a), the main peaks in all samples at 971 cm^{-1} are assigned to the asymmetrical stretching vibration of Si−O−Al at 3 days. It corresponds to the geopolymerization [43]. All the pastes show the similar degree of geopolymerization, which is due to the dissolved $Al(OH)_4^-$ at the early reaction stage by slag incorporation. It indicates that C(N)−A−S−H is produced in all pastes.

Simultaneously, the band at 778 cm^{-1} is associated with the symmetric stretching vibrations of Si−O−Si bridges from C(N)−A−S−H gels [44]. Similarly, a band at 664 cm^{-1} attributed to the symmetrical stretching of Si−O−T bonds is identified in the spectra of all samples [45]. It is also due to the C(N)−A−S−H gels in all samples. The peaks at 1432 and 880 cm^{-1} are associated with the stretching vibrations of CO_3^{2-} [46]. The intensity of CO_3^{2-} stretching peaks are more obvious in NH and NHNA samples, while the NA samples show thinner humps at these ranges. It is owing to more carbonated phases in NH and NHNA samples than that in NA samples. It is in good agreement with QXRD and TG results at 3 days. Particularly, the peaks in NA samples at 552 cm^{-1} are

Table 3
Thermodynamic data of paste samples at 3 days.

	40–100 °C	40–200 °C	100–300 °C	25–400 °C	700 °C	850 °C
NA3–3d	Moisture water	Zeolite A	C(N)−A−S−H			
	Mass losses during this range: 9.54 wt. %					
NA4-3d	Moisture water	Zeolite A	C(N)−A−S−H			
	Mass losses during this range: 9.56 wt. %					
NA5-3d	Moisture water	Zeolite A	C(N)−A−S−H			
	Mass losses during this range: 10.59 wt. %					
NHNA3–3d	Moisture water	Zeolite A	C(N)−A−S−H	Zeolite Na-P_1	Calcite	Natrite
NHNA4-3d	Moisture water	Zeolite A	C(N)−A−S−H	Zeolite Na-P_1	Calcite	Natrite
NHNA5-3d	Moisture water	Zeolite A	C(N)−A−S−H	Zeolite Na-P_1	Calcite	Natrite
NH3–3d	Moisture water		C(N)−A−S−H	Hydrotalcite	Calcite	Natrite
NH4-3d	Moisture water		C(N)−A−S−H	Hydrotalcite	Calcite	Natrite
NH5-3d	Moisture water		C(N)−A−S−H	Hydrotalcite	Calcite	Natrite

Table 4
Thermodynamic data of paste samples at 28 days.

	40–100 °C	40–200 °C	100–300 °C	25–400 °C	700 °C	850 °C
NA3–3d	Moisture water	Zeolite A	C(N)−A−S−H			
	Mass losses during this range: 10.11 wt. %					
NA4-3d	Moisture water	Zeolite A	C(N)−A−S−H	Zeolite Na-P_1		
	Mass losses during this range: 10.89 wt. %					
NA5-3d	Moisture water	Zeolite A	C(N)−A−S−H	Zeolite Na-P_1		
	Mass losses during this range: 11.5 wt. %					
NHNA3–3d	Moisture water	Zeolite A	C(N)−A−S−H	Zeolite Na-P_1	Calcite	Natrite
NHNA4-3d	Moisture water	Zeolite A	C(N)−A−S−H	Zeolite Na-P_1	Calcite	Natrite
NHNA5-3d	Moisture water	Zeolite A	C(N)−A−S−H	Zeolite Na-P_1	Calcite	Natrite
NH3–3d	Moisture water		C(N)−A−S−H	Hydrotalcite	Calcite	Natrite
NH4-3d	Moisture water		C(N)−A−S−H	Hydrotalcite	Calcite	Natrite
NH5-3d	Moisture water		C(N)−A−S−H	Hydrotalcite	Calcite	Natrite

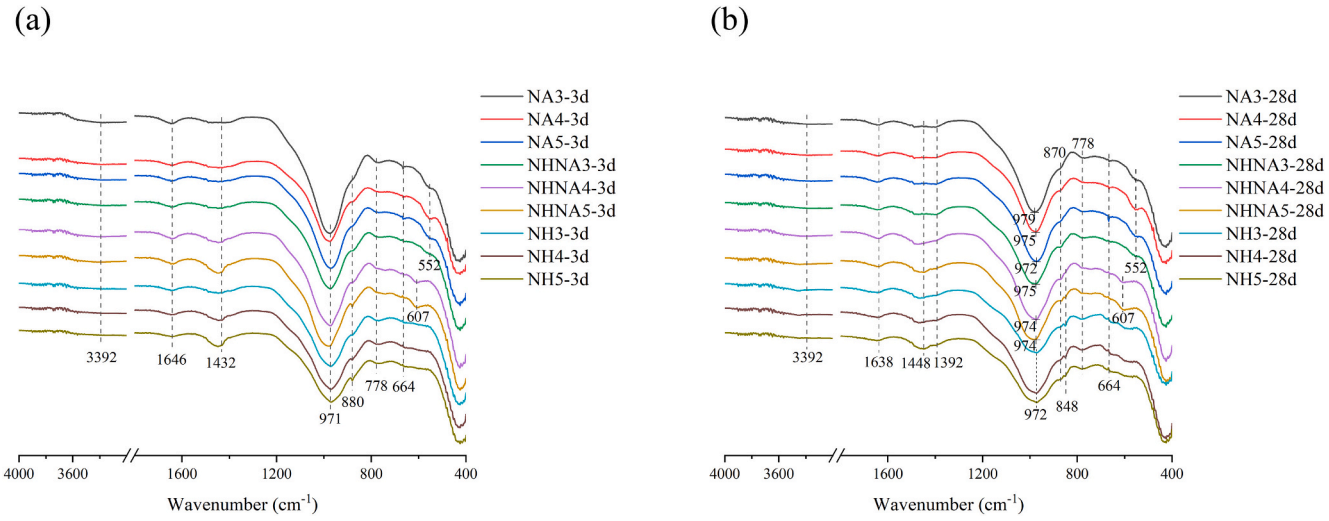

Fig. 4. (a) 3-day and (b) 28-day FTIR spectrum of SAASG.

attributed to the 8Si-D4R unit of zeolite A, which is the ring vibrations of the zeolite A structure [47,48]. This peak also shows a weak stretching vibration in NHNA3 pastes, because a small amount of zeolite A is observed in NHNA3 from XRD patterns. However, there is no presence of this peak in other NHNA and NH samples. It is due to the rather low content or absence of zeolite A in those samples, which is in line with XRD patterns. Besides, the stretch at 607 cm^{-1} in NHNA4 and NHNA5 is due to Si—O in bending modes from the zeolite Na—P_1 [49,50]. It is the primary zeolite formation in these specimens as described in XRD patterns. The peaks at 3392 and 1646 cm^{-1} are due to the stretching vibration of O − H from bound water molecules of the samples [21].

For 28-day FTIR spectra in Fig. 4 (b), a distinctive bending and shifting vibration of Si−O−Al from C(N)−A−S−H formation at around 972–979 cm^{-1}. The degree of geopolymerization increases with the curing ages. The NA3 pastes show the highest wavenumber (979 cm^{-1}) in this range, representing the highest degree of geopolymerization among the concerned specimens. At the same time, the wavenumbers in NA3 (979 cm^{-1}), NA4 (975 cm^{-1}), and NA5 (972 cm^{-1}) decrease with the equivalent Na_2O content. Similarly, the degree of geopolymerization in NHNA samples reduces with the equivalent Na_2O content. The peaks of the Si−O−Al bond in NH samples are at the same position (972 cm^{-1}). Moreover, the decrease of wavenumbers represents that more Al participates in C(N)−A−S−H formation with the higher equivalent Na_2O content [51]. This is because a high pH of the activator is beneficial to the dissolution of $Al(OH)^-_4$into the pore solution. More $Al(OH)^-_4$ can be adopted by the silicate chain forming a 3D structure of gels, which leads to a higher main chain length. Similarly, with 3-day samples, the peaks at 778 and 664 cm^{-1}, Si−O−Si bonds, and Si−O−T bonds from C(N)−A−S−H gels remain unchanged along with the curing ages. In addition, the bands at 1448 (ν_3), 1392 (ν_3), and 870 cm^{-1} (ν_2) are due to the presence of carbonate phases with different vibration modes [46]. These carbonate phases are from natrite and calcite, which is consistent with the XRD results. Especially, a band at 848 cm^{-1} in NHNA4, NHNA5, and all NH samples can be observed at 28-curing days. It is owing to CO_3^{2-} stretching vibration of magnesite [52]. It is also in line with the XRD results. The bands at 552 cm^{-1} assigned to the 8Si-D4R unit from zeolite A remain unchanged in NA3, NA4, NA5, and NHNA3. Meanwhile, the bands at 607 cm^{-1} from zeolite Na—P_1 also remain unchanged in NHNA4 and NHNA5. Also, the peaks at 3392 and 1638 cm^{-1} due to the stretching vibration of bound water molecules keep constant along the curing ages.

3.2. Gel structure

3.2.1. ^{29}Si MAS NMR

The ^{29}Si MAS NMR data of raw materials are shown in Fig. 5, and the parameters of their deconvolution fitting curves are listed in Table 5. The ^{29}Si MAS NMR data of anhydrous slag illustrate a single broad resonance with a maximum intensity at around −74.5 ppm (Fig. 5(a)). It represents a wide distribution of Si environment and chemical shifts of raw slag, which is compatible with amorphous nature of the material as shown by XRD. According to previous studies, the signal is associated with Q^0 units at −74 ppm [53,54]. The ^{29}Si MAS NMR data of anhydrous waste glass also show a single broad resonance with a maximum intensity at around −92.5 ppm (Fig. 5(b)). It represents a wide distribution of Si environments and chemical shifts of raw waste glass. The signal is associated with Q^1 units at −82.5 ppm, Q^2 units at −90 ppm, Q^3 units at

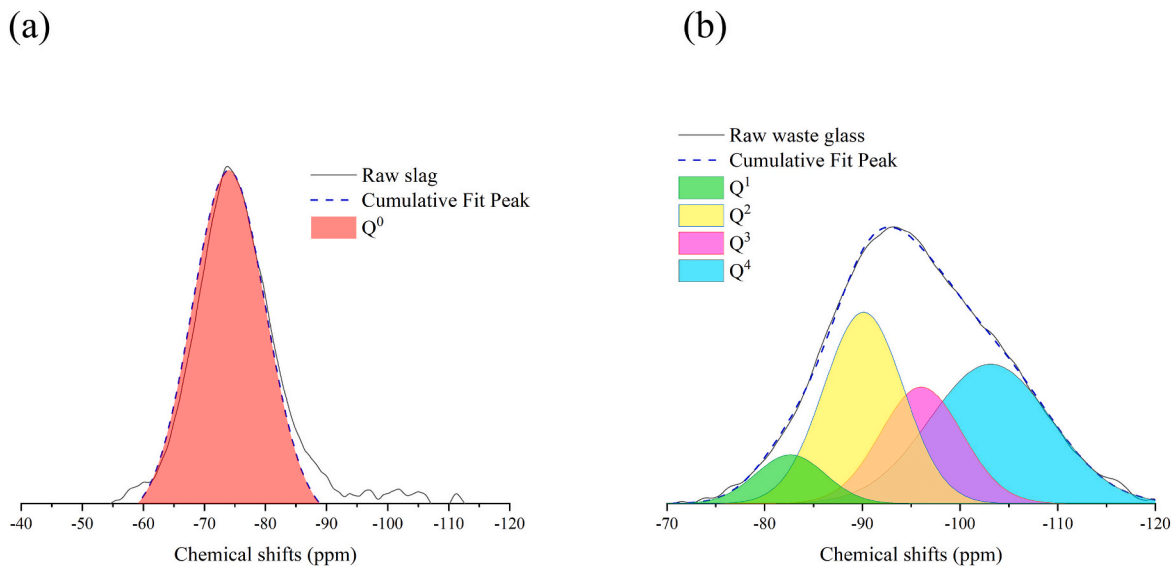

Fig. 5. ^{29}Si MAS NMR of raw materials (a) slag; (b) waste glass.

Table 5
^{29}Si MAS NMR of raw materials.

Sample		Q^0	Q^1	Q^2	Q^3	Q^4
Slag	Pos. (ppm)	−74	/	/	/	/
	Width[a]	14.2	/	/	/	/
	Integral (%)	100	/	/	/	/
Waste glass	Pos. (ppm)	/	−82.5	−90	−96	−103
	Width	/	8.4	9.6	9.9	14.6
	Integral (%)	/	7.5	33.8	21.2	37.5

[a] Width = Full width at half maximum.

−96 ppm, and Q^4 units at −103 ppm [26,55–57].

The ^{29}Si MAS NMR analyses of SAASG pastes at 3 and 28 days are shown in Fig. 6, and the parameters of their deconvolution fitting curves are listed in Table 6. Regardless of curing ages, the primary peaks are at −91 ppm for the Q^2(0Al) unit in NA, NHNA, and NH samples. Those peaks are attributed to the C(N)−A−S−H gels in NA and NHNA samples [27,54], and C−S−H gels in NH samples [26]. Notably, the sharp peaks at −89.1 ppm are assigned to the Q^4(4Al) unit of zeolite A in NA and NHNA samples [58]. However, no typical peak of the Q^4(4Al) unit can be observed in NH samples. This is because the extra $Al(OH)_4^-$ promotes the zeolite A formation in NA and NHNA samples, but insufficient $Al(OH)_4^-$ in NH samples results in the absence of zeolite A. Generally, more Q^2 and Q^3 silicate species mean a better solubility of slag and waste glass in the SAASG pore solution, which may further lead to different geopolymerization processes in the matrix.

For NA3 paste from 3 to 28 days, Q^2 and Q^3 are the mostly silicate species as shown in Fig. 6(a) and (b). The peak of Q^2(0Al) silicate is the highest at −91 ppm, and the peak of Q^2(1Al) silicate also shows a high intensity. Q^2(0Al) and Q^2(1Al) silicate species are the characteristic peaks of C(N)−A−S−H [27,54]. The high intensity of Q^2(1Al) and Q^3(1Al) silicate indicates that a large amount of $Al(OH)_4^-$ has replaced Si $(OH)_4$ in the bridging site of C−S−H, forming C−A−S−H [59]. Simultaneously, the partial replacement of Ca^{2+} by Na^+ leads to the formation of C(N)−A−S−H gels [21]. Besides, the decrease of Q^2(0Al) and Q^2(1Al) silicate species from 3 to 28 days is due to lower silicate MCL_{nc} of C(N)−A−S−H gels along the curing period as shown in Table 7. The decrease of MCL_{nc} of C(N)−A−S−H gels is due to the elevated incorporation of Ca^{2+} from slag and waste glass into gels [60]. It is also proved by the lower content of middle-chain silicate species (Q^2 and Q^3) and higher content of end-chain silicate specie (Q^1 represents silicate chain end). Less Q^2 and Q^3, more Q^1 silicate indicate the shortening of silicate chain from 3 days to 28 days. The peak at −82.5 ppm increases with the curing ages, which is associated with the increased amount of end-chain Q^1 silicate specie in C(N)−A−S−H gels [27]. It is attributed to the higher incorporation of Ca^{2+}, which leads to more end-chain Q^1 silicate species [61]. The resonances at −96.6 ppm and at −92 ppm are due to the Q^3(0Al) and Q^3(1Al) sites [62], which is attributed to the crosslinked C(N)−A−S−H gels formation in the paste. It is highly related to the MCL_c of C(N)−A−S−H gels. As can be seen from Table 7, the MCL_c of C(N)−A−S−H gels decreases with the curing ages, thanks to the higher Ca^{2+} incorporation in C(N)−A−S−H gels. No detection of Q^0 site in NA3 compared to raw materials indicates that Q^0 silicate has transferred to Q^1 or Q^2.

There is no obvious difference between NHNA3–3 days and NHNA3–28 days in terms of the silicate species group (Fig. 6(c) and (d)). Simultaneously, NHNA samples show the same chemical shift position as NA samples. It represents that the $NaAlO_2$ activator leads to a large quantity of C(N)−A−S−H gels formation in a low-Ca, high-Al environment [27]. Notably, the MCL_{nc} and MCL_c of NHNA3–28 days pastes are lower than that of NA3–28 days pastes up to 32.3 % and 41.5 %, respectively. It is associated with the high pH of the activator used in NHNA samples, because the higher pH value decreases the Al uptake by C−S−H, then less bridging Al can be introduced into the silicate chain [24]. Less Q^2 and Q^3, as well as more Q^1 silicate are observed at higher pH, which also indicates the shortening of silicate chain length. Eventually, NHNA samples form C(N)−A−S−H gels with shorter MCL than NA samples.

The NH3–3 days and NH3–28 days pastes exhibit typical C−S−H gels structure as shown in Fig. 6(e) and (f), which is different from $NaAlO_2$-activated matrix. The resonances at −91 ppm show the high intensity up to 35.8 % and 25.8 % at 3 and 28 days, respectively. Those characteristic resonances are associated with the Q^2(0Al) site from C−S−H gels in the matrix. Similarly, the signals of the Q^1(0Al) site at −82.5 ppm and Q^3(0Al) site at −96 ppm are also from the reflection of C−S−H gels. The peak at −85 ppm is associated with a small amount of C−A−S−H gels formation [59]. As can be seen from Table 7, a slight decrease in MCL can be observed along the curing ages. It is due to more dissolved Ca^{2+} incorporation that lessens the MCL of C−S−H gels. The MCL_{nc} of NH samples is lower than that of NA and NHNA samples. It is due to the absence of Al in NH samples leads to a lower MCL of C−(A)−S−H gels. This is also reported in previous studies [24,63].

Overall, the NA samples show a high extent of crosslinked formation, while the C(N)−A−S−H gels in NHNA samples exhibit a lower extent of the crosslinked structure. The NH samples illustrate the typical C−S−H/

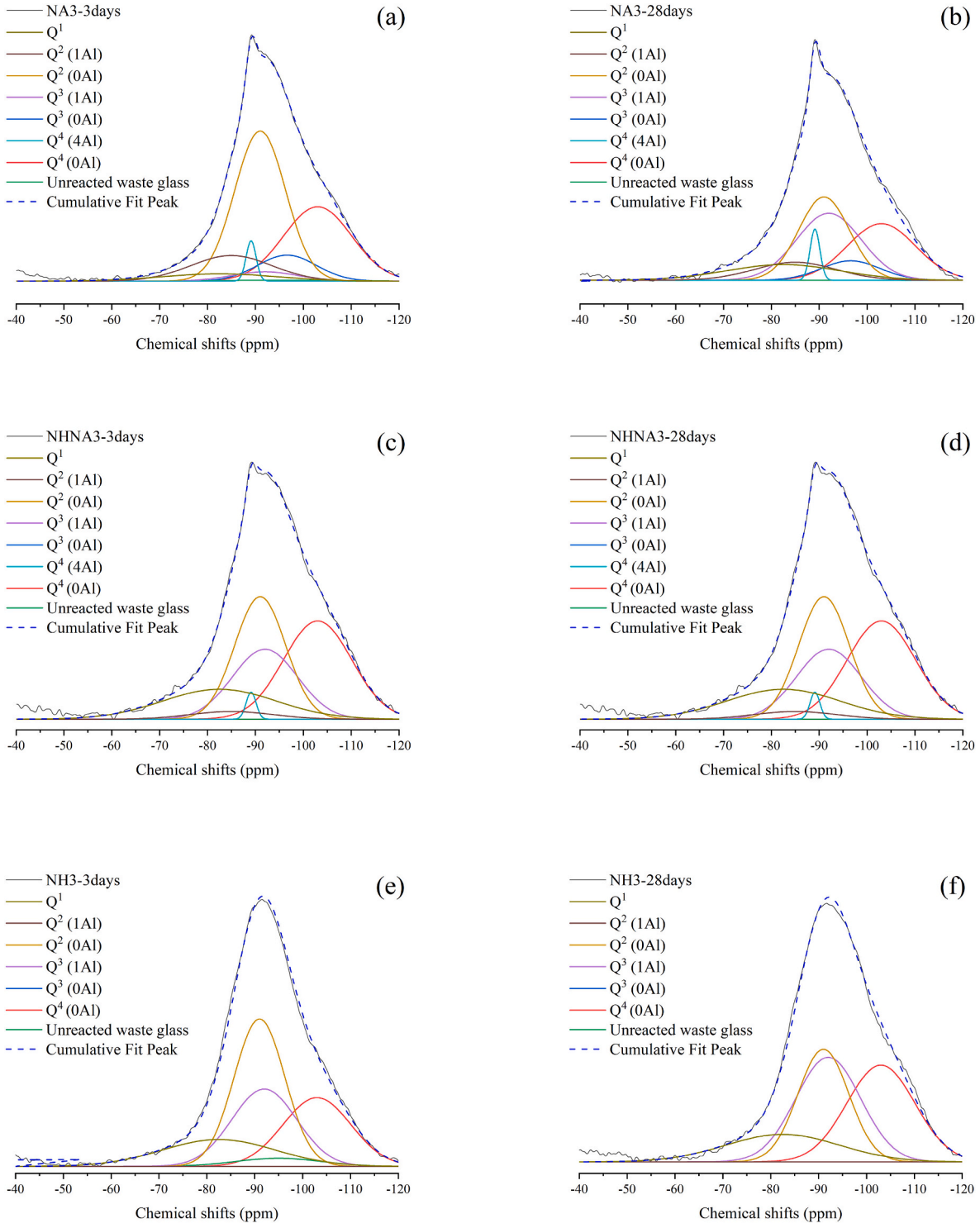

Fig. 6. ^{29}Si MAS NMR of SAASG at 3 and 28 days.

C−A−S−H gels formation, and its MCL is significantly lower than that of C(N)−A−S−H gels in NA samples. It confirms that the $NaAlO_2$ activation introduces extra $Al(OH)_4^-$ into the silicate chain. More bridging Al results in a longer MCL, further leading to more Na^+ ions bonding at silicate chain end (when Ca^{2+} ions are insufficient). This transfers the hydrated gels from C−(A)−S−H to C(N)−A−S−H.

3.2.2. ^{27}Al MAS NMR

The ^{27}Al MAS NMR data of raw materials are shown in Fig. 7, and the parameters of their deconvolution fitting curves are listed in Table 8. The ^{27}Al MAS NMR data of anhydrous slag illustrate a broad resonance at around 65 ppm (Fig. 7 (a)). It represents an Al[*IV*] site in the raw slag [64]. The resonance with a weak intensity at 10.3 ppm represents an Al [VI] site in the raw slag, which is similar to previous study [57]. The ^{27}Al MAS NMR data of anhydrous waste glass exhibit a broad resonance at around 57.5 ppm (Fig. 7 (b)), corresponding to Al[*IV*] site in the raw waste glass.

Three distinct Al environments (Al[IV], Al[V], and Al[VI]) of SAASG pastes at day 3 and 28 are detected in the ^{27}Al MAS NMR pattern (Fig. 8)

Table 6
^{29}Si MAS NMR of paste samples.

Sample		Q^1	Q^2 (1Al)	Q^2 (0Al)	Q^3 (1Al)	Unreacted waste glass	Q^3 (0Al)	Q^4 (4Al)	Q^4 (0Al)
NA3–3 days	Pos. (ppm)	−82.5	−85	−91	−92	−95	−96.6	−89.1	−103
	Width	28	20	12.5	16	21	14.5	2.45	16.78
	Integral(%)	4.5	11.4	41.9	3.3	0.6	8.4	2.2	27.7
NA3–28 days	Pos. (ppm)	−82.5	−85	−91	−92	−95	−96.6	−89.1	−103
	Width	28	20	12.5	16	21	14.5	2.45	16.78
	Integral(%)	10.3	8.5	24.4	25.1	0.1	6.6	2.9	22.2
NHNA3–3 days	Pos. (ppm)	−82.5	−85	−91	−92	−95	−96.6	−89.1	−103
	Width	28	20	12.5	16	21	14.5	2.45	16.78
	Integral(%)	15.7	2.9	28.6	20.9	0.01	0.1	1.2	30.6
NHNA3–28 days	Pos. (ppm)	−82.5	−85	−91	−92	−95	−96.6	−89.1	−103
	Width	28	20	12.5	16	21	14.5	2.45	16.78
	Integral(%)	15.7	2.9	28.6	20.9	0.01	0.1	1.3	30.6
NH3–3 days	Pos. (ppm)	−82.5	−85	−91	−92	−95	−96.6	/	−103
	Width	28	20	12.5	16	21	14.5	/	16.78
	Integral(%)	14.6	0.1	35.8	24	3.3	0.8	/	22.3
NH3–28 days	Pos. (ppm)	−82.5	−85	−91	−92	−95	−96.6	/	−103
	Width	28	20	12.5	16	21	14.5	/	16.78
	Integral(%)	14.1	0.1	25.8	30.6	3.3	0.9		25.2

Table 7
Mean chain length and Al—Si substitution of C(N) − A − S − H gel.

Groups	MCL_{nc}	MCL_c	Al-Si substitution
NA3–3 days	28.2	64.7	0.1
NA3–28 days	9.2	38.8	0.1
NHNA3–3 days	6.2	22.7	0.03
NHNA3–28 days	6.2	22.7	0.03
NH3–3 days	6.9	27.2	0.001
NH3–28 days	5.7	28	0.001

at 52–75 ppm, 39.8 ppm, and 5–15 ppm, respectively [65]. The parameters of their deconvolution fitting curves are listed in Table 9. The profile of the NMR spectra shows similarities between NA and NHNA samples including 4 Al[IV] sites at 75 (q^2[I]), 67 (q^2[II]), 59.4 (Al[IV]-2), and 57.5 (Al[IV]-1) ppm, which is consistent with the dissolution of raw materials and the formation of aluminosilicate reaction products (zeolite and C(N)−A−S−H gels). The presence of Al[V] corresponds to the crosslinked C(N)−A−S−H gels structure as reported in the previous studies [60,61], while Al[VI] represents different reaction products varying in NA and NH samples, corresponding to zeolite [66] or hydrotalcite [65], respectively. Particularly, the NA samples have a significantly high zeolite A peak while the NHNA samples show lower zeolite A intensities. It is due to that the solo $NaAlO_2$ activator promotes the Al species incorporation in the formation of zeolite A.

Fig. 8 (a) and (b) show the ^{27}Al MAS NMR analysis of the NA3 sample from 3 to 28 days. The q^2 aluminate species at 75 and 67 ppm are assigned to two different local environments q^2[I] and q^2[II], respectively. Meanwhile, the resonance at 57.5 ppm is assigned to Al[IV]-1 site. These locations have been attributed by previous investigations to Al replaced into paired tetrahedra in C(N)−A−S−H gels [67]. The deconvolutions also show high intensity at 62 ppm corresponding to q3, which means high levels of cross-linking in the C(N)−A−S−H gels structure. It is also in agreement with the ^{29}Si MAS NMR analysis. Typically, the Al[IV]-2 aluminate species at 59.4 ppm are associated

Table 8
^{27}Al MAS NMR of raw materials.

Sample		Al[IV]	Al[VI]
Slag	Pos. (ppm)	65	10.3
	Width*	26.50	9.00
	Integral (%)	96.71	3.29
Waste glass	Pos. (ppm)	57.5	/
	Width	17.20	/
	Integral (%)	100	/

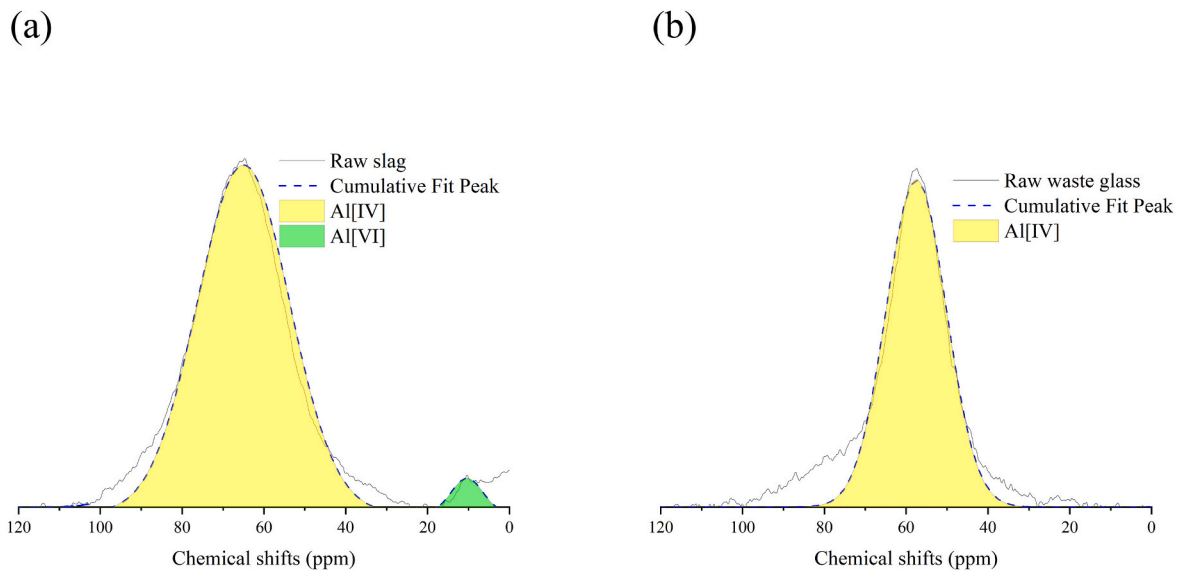

Fig. 7. ^{27}Al MAS NMR of raw materials (a) slag; (b) waste glass.

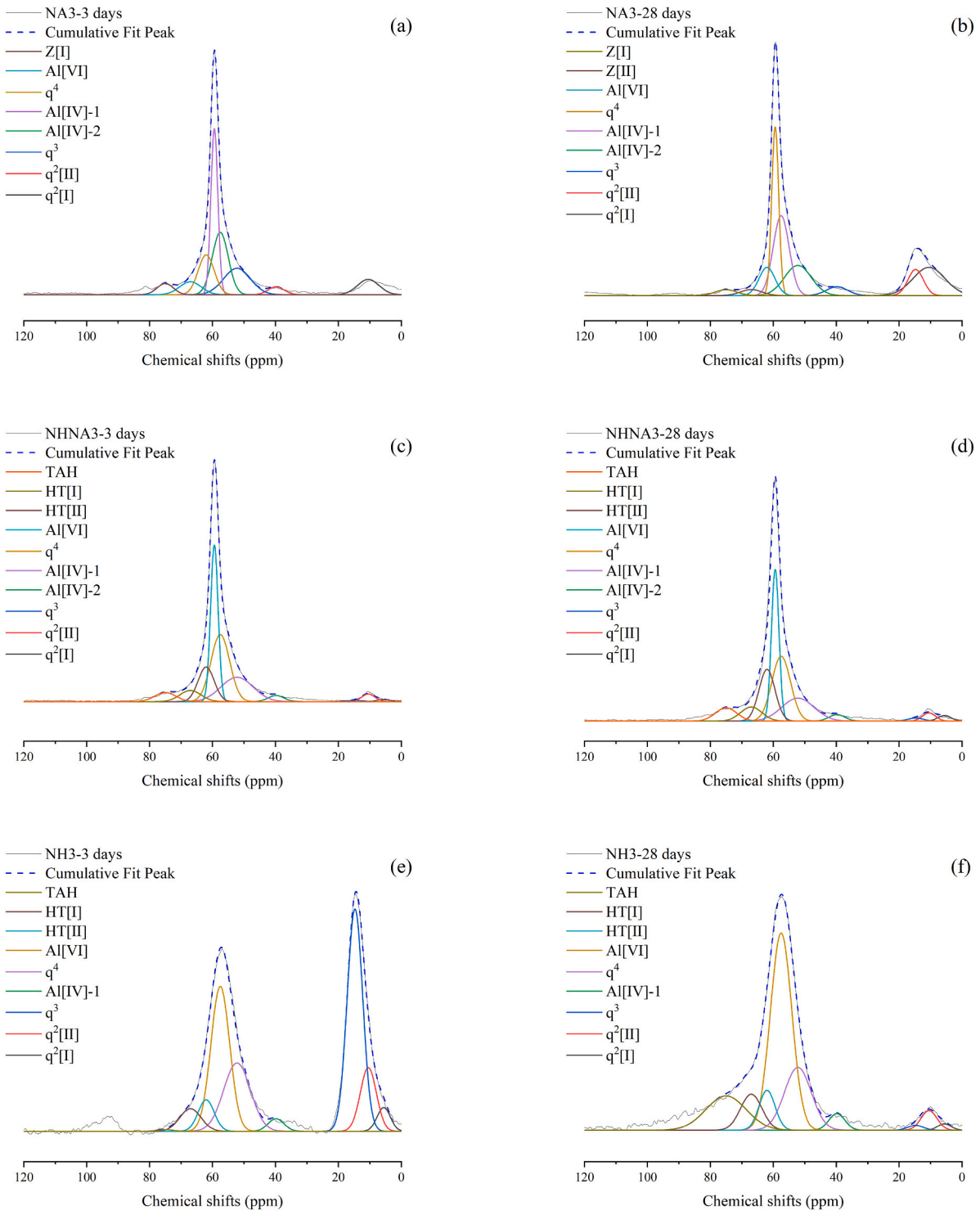

Fig. 8. ^{27}Al MAS NMR of SAASG at 3 and 28 days.

with tetrahedral Al in zeolite A [68]. Simultaneously, the Z[I] peak at 10.5 ppm is from the octahedral Al zeolite A [66]. The Z[II] aluminate species (octahedrally coordinated Al) at 14.7 ppm increases with the curding ages shown in Table 9. It represents that the tetrahedrally coordinated Al of zeolite A transfers to octahedrally coordinated Al [69]. It is due to the change in the Al chemistry of the activated system. The decrease of pH environment in the pore solution leads to more presence of octahedrally coordinated Al, leading to more octahedrally coordinated Al in zeolite A. The q^4 sites at 52.5 ppm are assigned to Q^4(4Al) owing to the zeolite A [65].

The NHNA3 samples show a limited increase of 2 Al[IV] sites (75, and 67 ppm) from 3d- to 28d-curing days (Fig. 8 (c) and (d)), representing a similar level of cross-linking in the C(N)−A−S−H gels. It is in line with ^{29}Si MAS NMR results. It is worth mentioning that the slight increase of Al[VI] aluminate species at 5.6 ppm suggests the existence of a third aluminate hydrate (TAH) [70]. It is intimately associated with the formation of C−S−H gels [71]. This is caused by the participation of NaOH that promotes the formation of the C−S−H gel.

Besides, the chemical state of Al in NH3 at 3 and 28 days shows the highest resonance at 57.5 ppm corresponding to C−S−H gels (and a

Table 9
^{27}Al MAS NMR of paste samples.

Sample		q^2[I]	q^2[II]	q^3	Al[IV]-2	Al[IV]-1	q^4	Al[V]	Z[II]/HT[II]	Z[I]/HT[I]	TAH
NA3–3 days	Pos. (ppm)	75	67	62	59.4	57.5	52.2	39.8	/	10.5	/
	Width	6	8	6	2.6	6	10	6	/	8	/
	Integral(%)	4.12	6.32	14.46	26.13	22.64	15.99	2.86	/	7.48	/
NA3–28 days	Pos. (ppm)	75	67	62	59.4	57.5	52.2	39.8	14.7	10.5	/
	Width	8	8	6	2.6	6	10	8	5.8	12	/
	Integral(%)	2.30	2.35	8.29	21.53	23.54	14.84	3.43	7.42	16.29	/
NHNA3–3 days	Pos. (ppm)	75	67	62	59.4	57.5	52.2	39.8	14.7	10.5	5.6
	Width	8	8	6	2.8	7	12	6	5.8	5	5
	Integral(%)	4.41	5.38	12.46	26.27	28.14	17.60	2.27	0.50	2.31	0.67
NHNA3–28 days	Pos. (ppm)	75	67	62	59.4	57.5	52.2	39.8	14.7	10.5	5.6
	Width	8	8	6	2.8	7	12	6	5.8	5	5
	Integral(%)	5.88	6.23	17.14	23.44	25.07	15.27	2.17	1.02	2.25	1.54
NH3–3 days	Pos. (ppm)	75	67	62	/	57.5	52.2	39.8	14.7	10.5	5.6
	Width	6	8	6	/	7	10	6	5.8	6	5
	Integral(%)	0.24	4.58	4.80	/	25.72	17.35	1.92	32.68	9.70	3
NH3–28 days	Pos. (ppm)	75	67	62	/	57.5	52.2	39.8	14.7	10.5	5.6
	Width	15	8	6	/	8	10	6	5.8	6	5
	Integral(%)	13.61	8.17	6.79	/	44.74	17.83	2.82	0.80	3.34	1.90

small amount of C−A−S−H gels) as shown in Fig. 8 (e) and (f). Meanwhile, the TAH site (in NH samples) at 5.6 ppm shows the highest intensity among the SAASG samples. As mentioned above, it is intimately related to the formation of the C−S−H gel. It suggests that the C−S−H is the primary gel type in NH samples. In addition, the resonances at 14.7 and 10.5 ppm are assigned to HT[II] and HT[I] sites, relating to the formation of hydrotalcite [65]. The remarkable decrease of HT[II] and HT[I] sites is associated with the transformation of the hydrotalcite phase into TAH during the curing ages.

In summary, based on the ^{29}Si and ^{27}Al MAS NMR results, the $NaAlO_2$ activator significantly contributes to a higher Al substitution for Si. It leads to a higher amount of Q^3 (1Al) of Si-species formation, transferring the primary gel formation from C−(A)−S−H to C(N)−A−S−H. It potentially enhances the Na participation into gels. Simultaneously, the Al participation increases the mean chain length of gels, and more crosslinked gel structures are obtained. The extra Al also transfer the hydrotalcite formation into TAH during curing.

3.3. Characterization of microstructure and mineralogy

Fig. 9 and Fig. 10 show the SEM micrographs of SAASG pastes at 3 and 28 days, respectively. The $Si(OH)_4$ and $Al(OH)_4^-$ species are released once the slag and waste glass specifies are in contact with the alkaline solutions [72]. As shown in Fig. 9 and Fig. 10, the unreacted slag and waste glass particles are adhered to the C(N)−A−S−H gels. The micro cracking increases with the elevated equivalent Na_2O content, which is caused by the high alkalinity of the matrix that leads to a higher risk of efflorescence. A higher extent of carbonation results in a looser microstructure, and more micro cracks are formed during the carbonation of activated waste glass. Notably, the NA pastes show the most refined microstructure among the samples. This is because the $NaAlO_2$ activator promotes the formation of C(N)−A−S−H gels by providing extra $Al(OH)_4^-$ species Moreover, the formation of C(N)−A−S−H gels reduces the risk of efflorescence. More Ca and Na are captured by $Al(OH)_4^-$ to form C(N)−A−S−H gels, limiting the calcite and natrite formation. Thereby, it reduces calcite and natrite formation during the air curing period. Compared to C(N)−A−S−H gels, these carbonate-phases have a relatively looser microstructure. The increase of micro cracking along the curing ages may be also related to carbonation.

Fig. 11 and Fig. 12 illustrate the quaternary phase (Si-Al-Ca-Na) diagrams and their projection maps of SAASG in molar ratio at 3 and 28 days, respectively. As shown in Fig. 11, the calcium-poor C(N)−A−S−H gels can be observed among the samples at 3 curing days. Because the waste glass is poor in calcium content, the Ca^{2+} is mainly dissolved from slag (10 wt% in precursors). The limited Ca^{2+} resource leads to the formation of calcium-poor C(N)−A−S−H gels. Besides, C(N)−A−S−H gels in NA and NHNA samples show a similar Al content (nearly 25 % elemental ratio), which is close to the maximum possible value in C(N)−A−S−H gels. Because only limited Al can replace Si sites to form geopolymers [73,74]. While in NH samples, low Al can be found in C(N)−A−S−H gels (lower than 5 % elemental ratio). It is due to very limited Al resources from slag (without $NaAlO_2$ supplement). The reaction products of the NH samples are easier to face efflorescence, so more Na_2CO_3 and $CaCO_3$ can be observed. It is worth mentioning that the sodium-poor C(N)−A−S−H gels can be observed in the NA3 sample, which is mainly caused by the low alkalinity and relatively low sodium aluminate.

It can be seen from Fig. 12, that the reaction products in 28-d NA and NHNA samples show that more calcium and sodium are incorporated in C(N)−A−S−H gels. With the curing ages, more and more $Si(OH)_4$ and Ca^{2+} dissolve from waste glass and slag and react with $Al(OH)_4^-$ from $NaAlO_2$ activator to form the C(N)−A−S−H gels. Compared to Na^+, Ca^{2+} has higher molecular weight and positive charges, it leads to more Ca^{2+} entering C(N)−A−S−H gels. The NMR results show that MCL_{nc} of NA and NHNA samples decrease along the curing ages, which is due to the Ca^{2+} participation. Previous studies also report that a higher calcium in the geopolymers leads to a shorter silicate chain length [75–77]. While the NH samples generate a large quantity of Na_2CO_3, $CaCO_3$, and C−(A)−S−H gels at 28 days. The scatters with low Al content in NH samples represent low content of C(N)−A−S−H gels in NH samples. This is in line with the NMR results. Besides, the Ca^{2+} from slag is beneficial to the development of microstructure. More Ca^{2+}-rich gels form and fill the pores in the matrix as previous study reported [78]. A denser microstructure of the matrix can be obtained by introducing more calcium-rich raw materials (e.g. slag). It is worth mentioning that the Si/Al ratio of one zeolite crystal should be similar to the one in the cementitious gel surrounding the zeolite crystal [79,80]. The gels compositions of NA samples show higher Al content than that of NHNA samples at 28 days in Fig. 12. At the same time, the major zeolite type in NA samples is zeolite A ($Na_{96}Al_{96}Si_{96}O_{384}{\cdot}216H_2O$), and in NHNA samples is zeolite Na—P_1 ($Na_6Al_6Si_{10}O_{32}{\cdot}12H_2O$). The Al/Si ratio of the zeolites are 1/1 and 3/5, respectively. It means that zeolite A has a higher Al/Si ratio than zeolite Na—P_1. It is in line with the EDS results of gel compositions. The Al/Si ratios of gel and zeolite A in NA samples are both higher than the Al/Si ratios of gel and zeolite Na—P_1 in NHNA samples. It is due to the extra Al participation in the formation of reaction products.

3.4. Efflorescence evaluation

3.4.1. Visual efflorescence observation

Fig. 13 exhibits clearly that NA3–56 days shows the lowest extent of efflorescence, while NH5–56 days shows the highest extent of

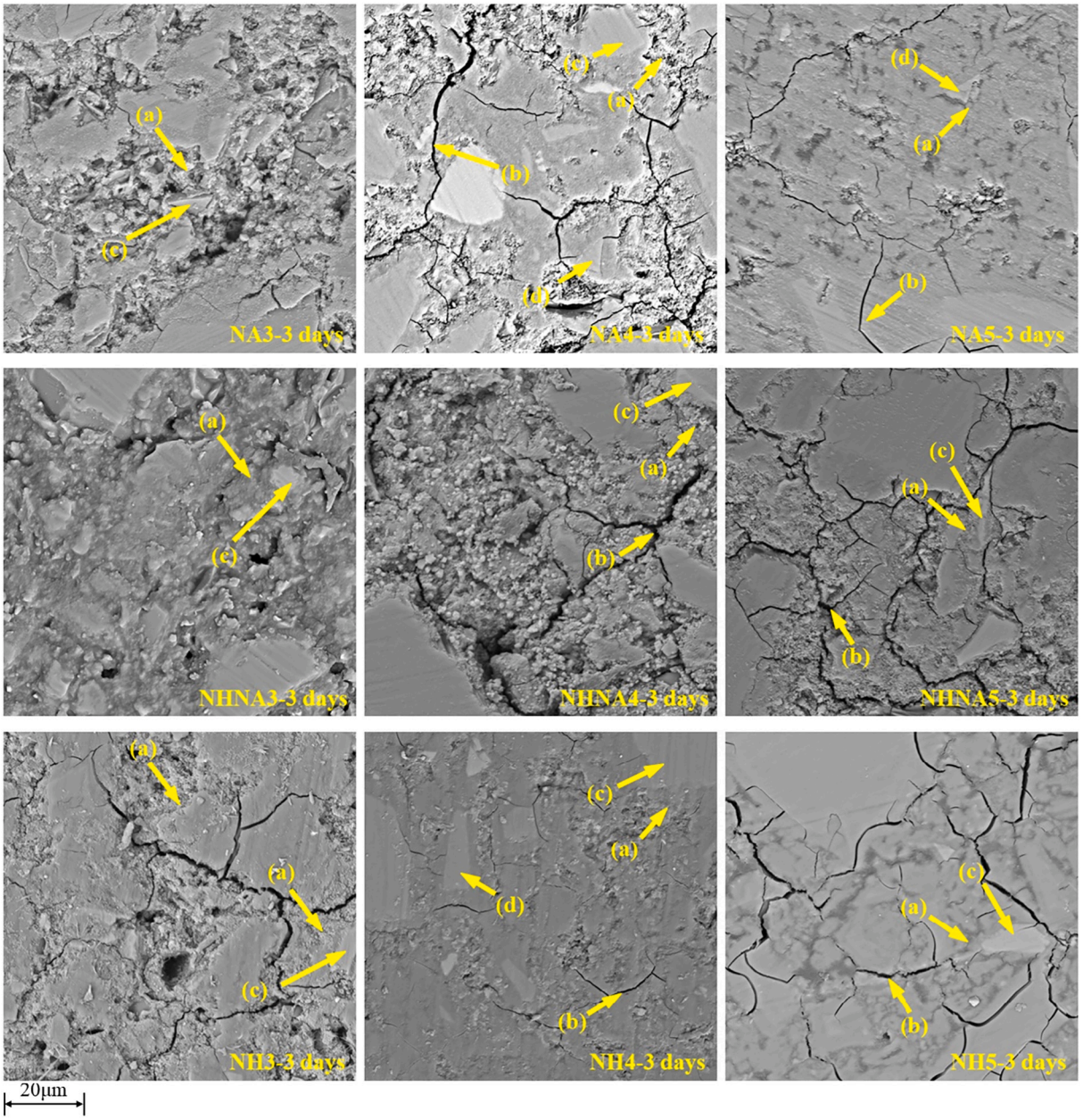

Fig. 9. SEM micrographs of SAASG at 3 days (a) C(N)−A−S−H gel; (b) Micro cracking; (c) Unreacted waste glass; (d) Unreacted slag.

efflorescence among the SAASG pastes at 56 days. The visual efflorescence of each paste as a function of curing ages is presented in Fig. A1. The extent of visual efflorescence increases with the equivalent Na_2O content. It is associated with a higher pH environment of the pastes. Compared to NA samples, the NH samples show an obviously more intensive efflorescence. It is associated with the leaching of Na^+ from the matrix. The NH samples possess more free Na^+ ions than the NA samples. The presence of $Al(OH)_4^-$ (in NA samples) from $NaAlO_2$ reduces the extent of efflorescence by forming more C(N)−A−S−H gels. It can bond more free Na^+ ions than NH samples. Besides, NA3 shows the lowest extent of efflorescence because the primary reaction product of NA3 is Na-rich *C(N)−A−S−H* gels. Therefore, less Na^+ ions are available to leach out from the matrix during the efflorescence test process.

3.4.2. *Indicative efflorescence results*

Fig. 14 shows the indicative efflorescence test results of SAASG pastes at 28- and 56-day air curing process. The statistics are overall in agreement with the levels of visible efflorescence in Fig. 13. As can be seen from Fig. 14, the pastes show a higher extent of alkali leaching with a higher equivalent Na_2O content. This is in consistence with the well-established tendency in pore solution chemistry, i.e. increasing the Na_2O content results in an enhanced alkalinity of the pore solution [11,81]. Subsequently, more free Na^+ ions can be diffused during the efflorescence process. At the same time, the higher Na_2O concentration also increases the dealumination of Al in C(N)−A−S−H gels [82]. Thus, it leads to a higher extent of efflorescence. In addition, NA3 samples show the lowest extent of efflorescence among the samples. The low alkali concentration of NA3 among the samples provides the lowest free alkali ions in the pore solution. Simultaneously, the extra $Al(OH)_4^-$ transfer the reaction products from C−(A)−S−H to C(N)−A−S−H gels. The longer MCL of $^{C(N)-A-S-H}$ captures more free Na^+ ions, mitigating the degree of efflorescence (this will be discussed in Sections 4.1 and 4.2). However, the hybrid activator group (NHNA5) shows an even higher extent of efflorescence when Na_2O is 5 wt%. This is caused by the increased micro cracks with the lowest compressive strength. The poor microstructure leads to the strongest tendency towards efflorescence,

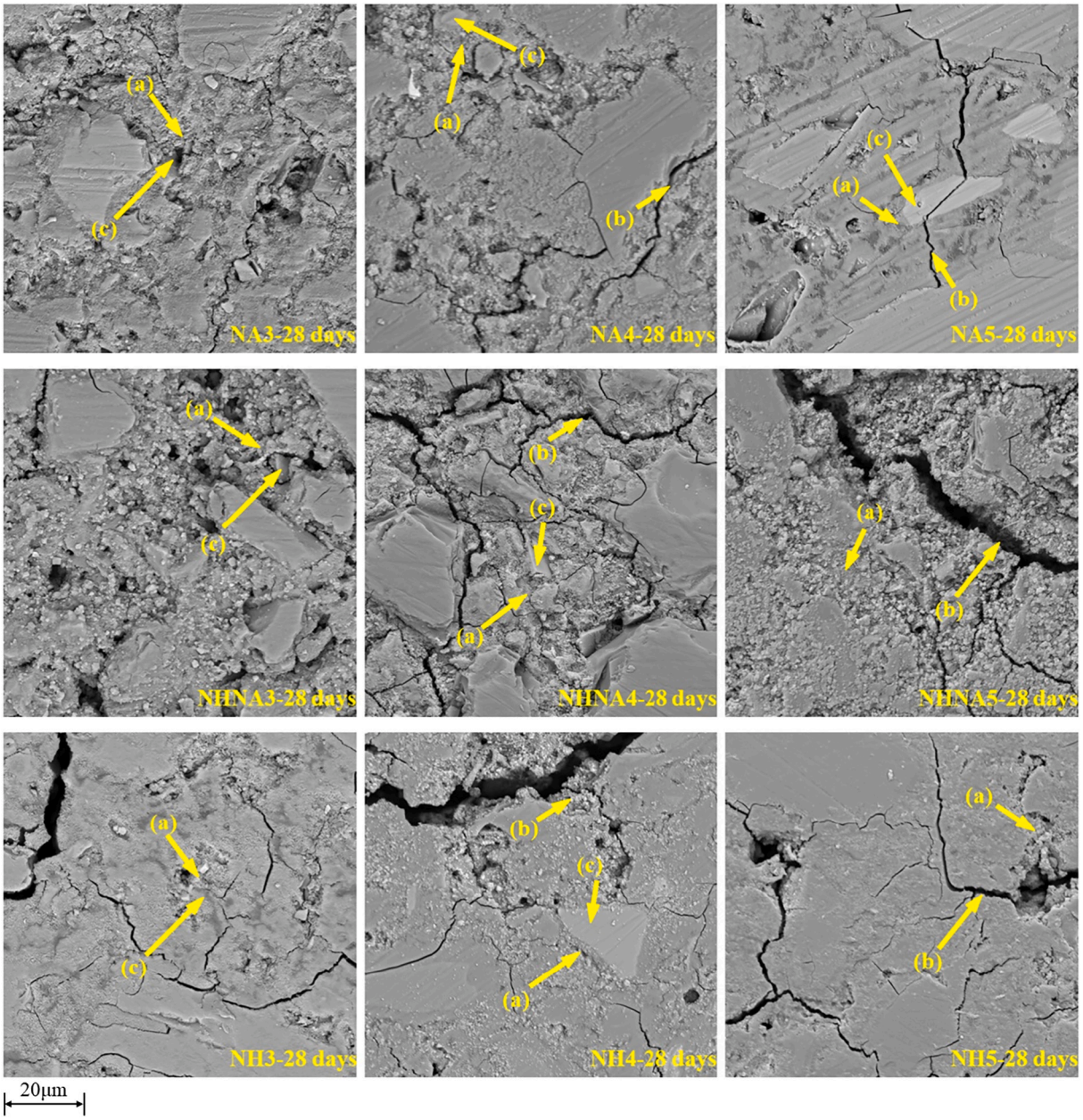

Fig. 10. SEM micrographs of SAASG at 28 days (a) C(N)−A−S−H gel; (b) Micro cracking; (c) Unreacted waste glass; (d) Unreacted slag.

where free alkali ions can easily transport to the surface of the paste.

3.5. Compressive strength

The compressive strength of SAASG pastes are displayed in Fig. 15 from 3 days up to 28 days. NA samples group consistently has the highest compressive strength at all ages, followed by the NH group and NHNA group. The high compressive strength of NA pastes can be ascribed to its large amount of C(N)−A−S−H formation, leading to a denser matrix [9,82]. Besides, the NA samples show the lowest efflorescence extent, which means less carbonation. The higher degree of carbonation in NH and NHNA groups leads to lower compressive strength as well [83]. The solo activators (NA or NH) show that a higher alkali concentration leads to a lower compressive strength. The greater alkalinity in the alkali activated waste glass system tends to have a higher content of ionic species. It impedes the mobility of ions, thereby procrastinating the polycondensation process. Consequently, the compressive strength is lowered [15,84]. However, the higher alkali concentration in the hybrid activator increases the compressive strength. It may be associated with a large amount of zeolite Na—P_1 formation consuming mostly the alkali ion and extra $Al(OH)_4^-$. Moreover, the higher alkalinity is beneficial to the geopolymerization process in NHNA samples. On the other hand, more zeolite Na—P_1 formation lessens the alkali ion and $Al(OH)_4^-$ participating in the formation of gels. Compared to NA and NH systems, less formation of gel results in the lowest strength.

4. Discussion

This study assesses the possibility of using sodium aluminate to tackle the efflorescence of activated waste glass and slag blends. The $NaAlO_2$ activator transferred the gelation from conventional C−(A)−S−H to C(N)−A−S−H that strongly helps to inhibit the intensive efflorescence of alkali activated waste glass (AAWG). At the same time, the relatively low pH of $NaAlO_2$ activator (compared to NaOH) also reduces the potential of efflorescence. Moreover, the present findings showed

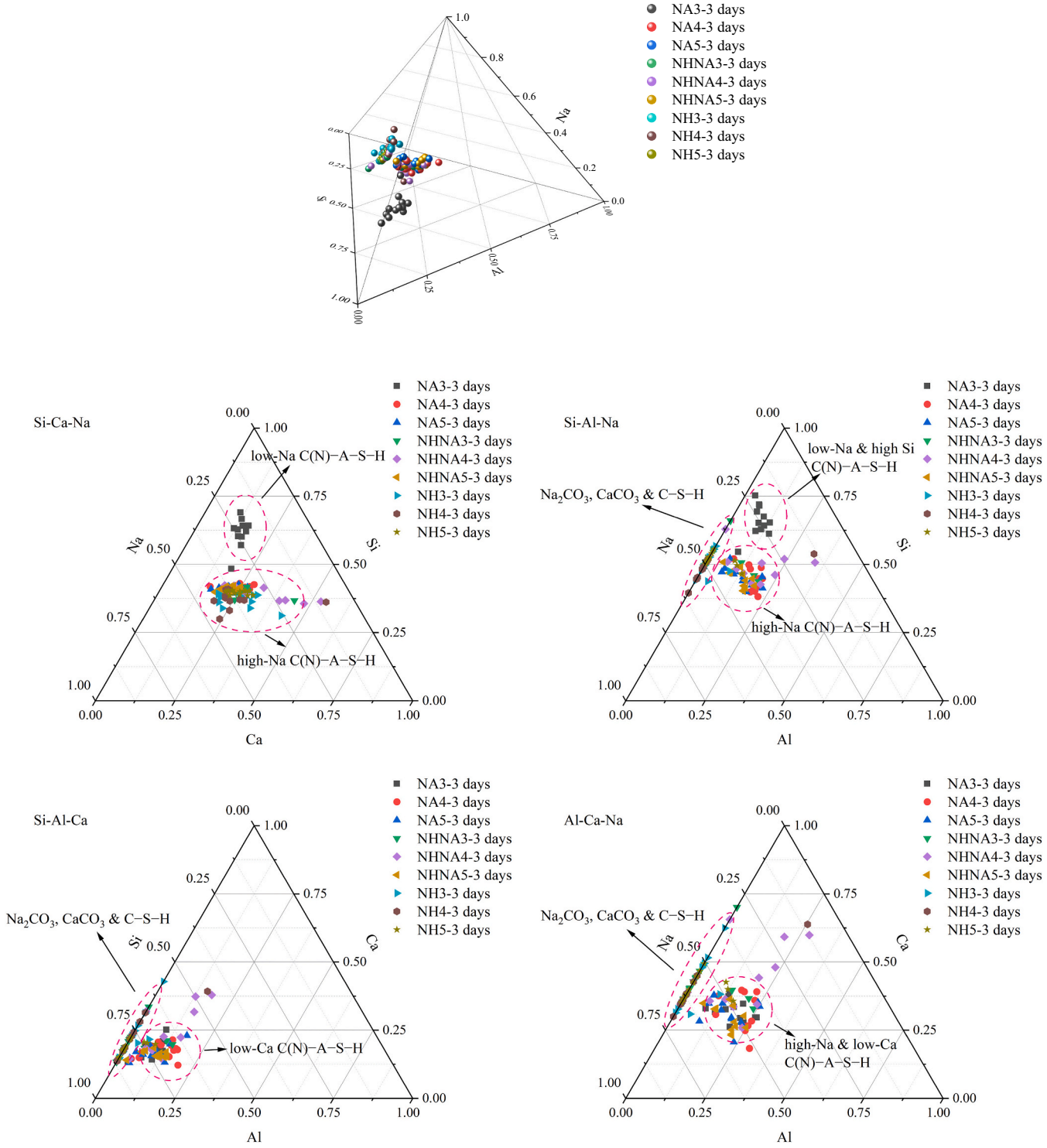

Fig. 11. Quaternary phase (Si-Al-Ca-Na) diagrams and its projection maps of activated slag and waste glass powder in molar ratio at 3 days.

that the sodium aluminate activated slag and waste glass (SAASG) exhibited high mechanical strength.

4.1. *Effect of* $Al(OH)_4^-$ *on the formation of gels in activated waste glass*

Fig. 16 exhibits the effect of $Al(OH)_4^-$ on the formation of gels in activated slag and waste glass. On the one hand, more free $Al(OH)_4^-$ in the pore solution leads to more content of $Q^2(1Al)$ and $Q^3(1Al)$ in the formation of gels according to the results in ^{29}Si MAS NMR. It represents more bridging Al in the gels, leading to longer MCL. The longer silicate chain indicates that potentially more hydrogen can be replaced by cations (like Ca^{2+} and Na^+) at the chain end. Since there is limited Ca^{2+} source in the SAASG, more Na^+ can replace hydrogen site. Then the formation of gels transfers from C−(A)−S−H to C(N)−A−S−H. On the other hand, the relatively low pH of solo $NaAlO_2$ than solo NaOH (or hybrid activator) is beneficial for the substitution of Si site by Al in the gels. This can be explained by the decreased pH that changes the spectra of tetrahedral Al(IV) but less for octahedrally bound Al(VI) [24]. More tetrahedral Al(IV) is available to uptake by silicate chain. It is also reflected in the ^{29}Si MAS NMR results. This leads to the long-chain-length

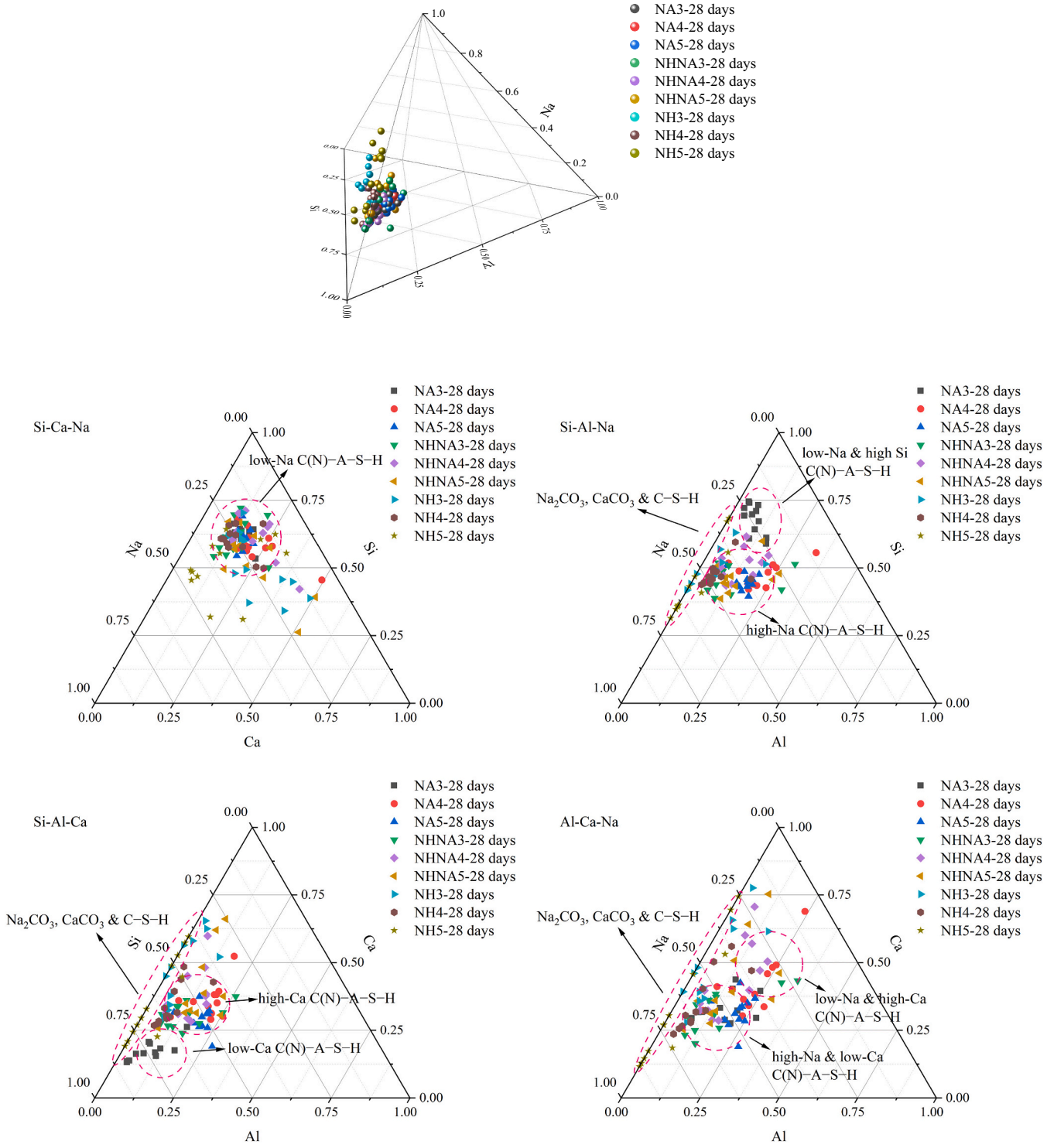

Fig. 12. Quaternary phase (Si-Al-Ca-Na) diagrams and its projection maps of activated slag and waste glass powder in molar ratio at 28 days.

gels. More Na^+ ions have higher possibility to incorporate into gels when Ca^{2+} ions are insufficient in the matrix.

Overall, the extra $Al(OH)_4^-$ species and the relatively low pH in the pore solution are the keys to transform the gels from C−(A)−S−H to C(N)−A−S−H in the activated glass system. Consequently, the sodium species are chemically steadier in the matrix.

4.2. *Effect of $NaAlO_2$ on efflorescence in activated glass*

Fig. 17 represents the influence of gels formation on the efflorescence process of NaOH and $NaAlO_2$ activated slag and waste glass. The $NaAlO_2$ activator provides extra $Al(OH)_4^-$ that promote the geopolymerization. At the same time, the participation of $Al(OH)_4^-$ monomers at the bridging sites of the silicate chain drives the Na^+ adopted by C−A−S−H to form C(N)−A−S−H gels [75]. Thus, the $NaAlO_2$ activator effectively stimulates $Al(OH)_4^-$ and Na^+ to occupy the silicate and calcium sites, respectively. It results in the crosslinked C(N)−A−S−H gel structure in $NaAlO_2$ activated matrix. Consequently, a large amount of free Na^+ ions are captured by the C(N)−A−S−H gels, resulting in a high resistance towards efflorescence. Generally, NaOH activated matrix lacks the

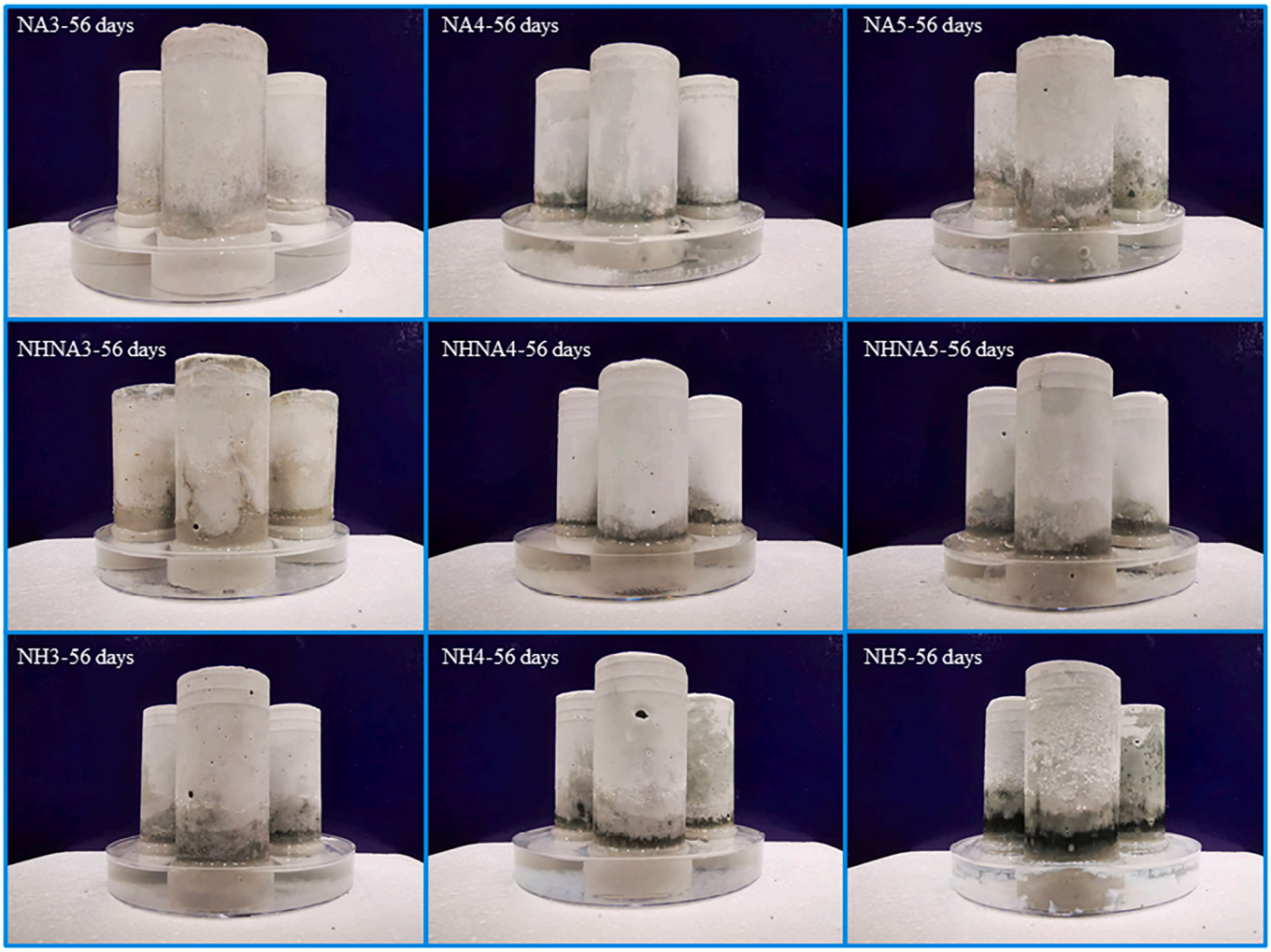

Fig. 13. Visual efflorescence testing SAASG pastes at 56 days.

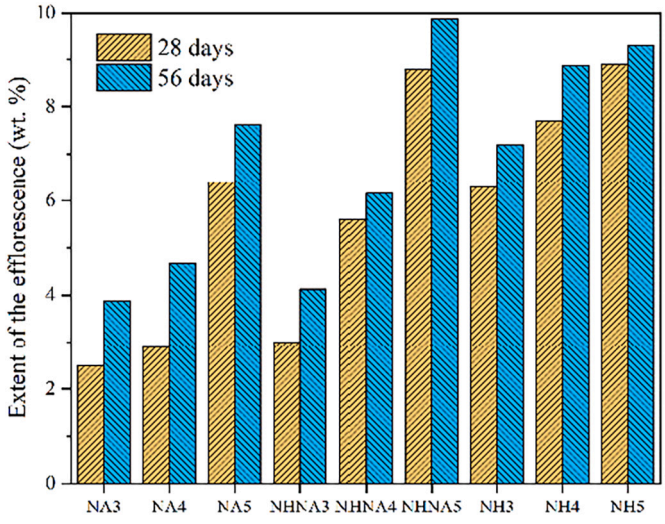

Fig. 14. Efflorescence testing of sodium hydroxide and sodium aluminate activated slag and waste glass at 28 and 56 days.

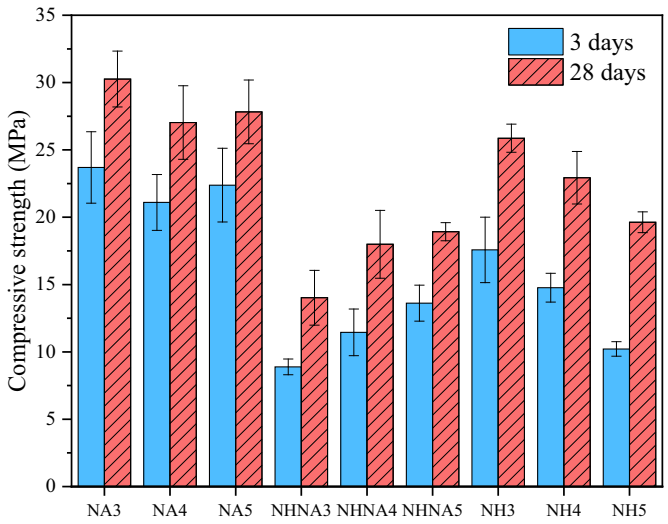

Fig. 15. Compressive strength of sodium hydroxide and sodium aluminate activated waste glass pastes at 3 and 28 days.

$Al(OH)_4^-$ monomers, the primary reaction products are C–(A)–S–H gels. Consequently, the numerous free Na^+ ions in the pore solution are at high risk of leaching. Simultaneously, the high alkalinity of NaOH activated matrix has a higher potential to face the carbonation issue. Thereby, the resistance of NaOH activated matrix towards efflorescence is relatively lower than that of $NaAlO_2$ activated matrix.

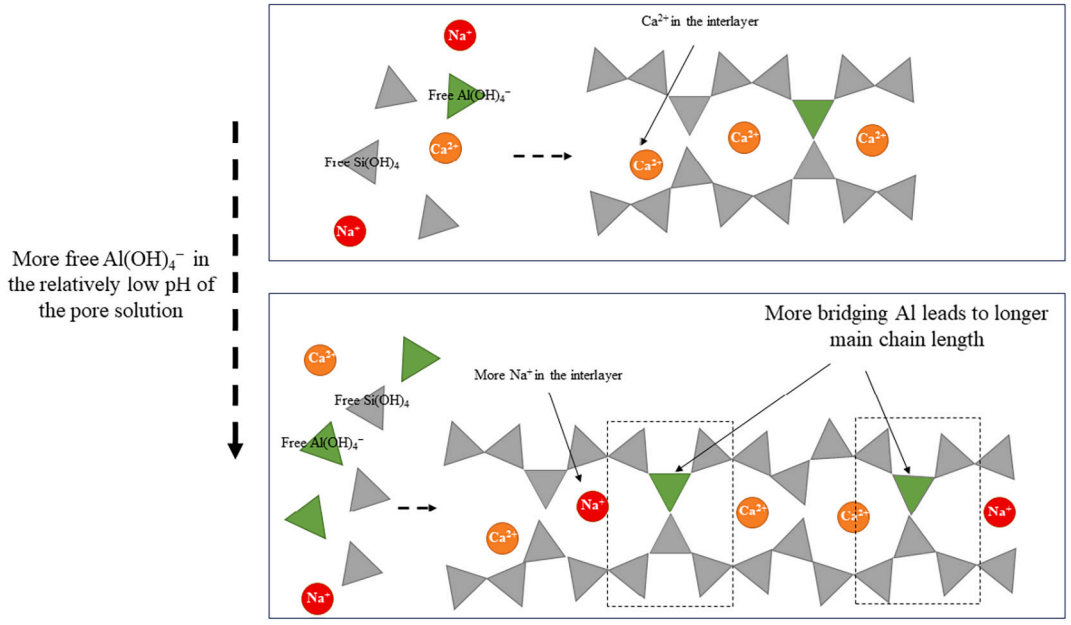

Fig. 16. Effect of $Al(OH)_4^-$ on the formation of gels.

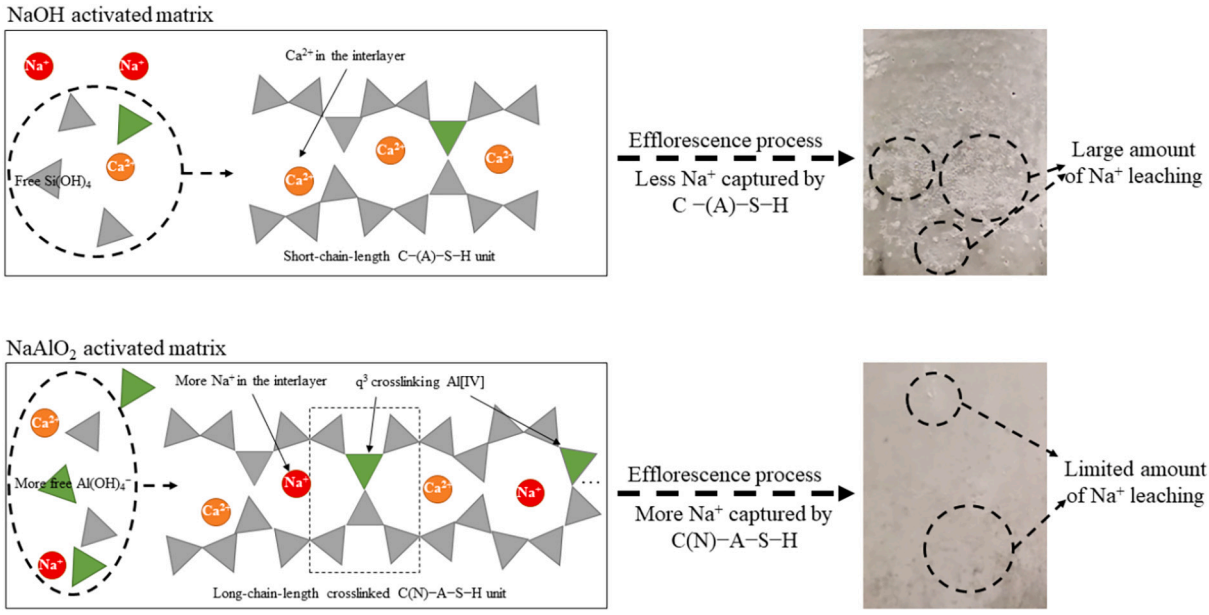

Fig. 17. Efflorescence process of NaOH and $NaAlO_2$ activated slag and waste glass.

Nevertheless, the C(N)−A−S−H gel content in the matrix is still difficult to quantify. Therefore, the quantitative influence of the $NaAlO_2$ activator is hard to evaluate. Investigating methods to quantify the C(N)−A−S−H gels formation would be of scientific and practical interest in controlling the efflorescence behavior in the future.

5. Conclusions

This study utilizes the sodium aluminate to activate waste glass and slag blends to mitigate the efflorescence behavior. Results show that the sodium aluminate provides extra $Al(OH)_4^-$ that promote the formation of C(N)−A−S−H gels in a relatively low pH environment. The formed C(N)−A−S−H gels have longer MCL that can capture more Na^+ that significantly improves the resistance of efflorescence (less free Na^+ in the pore solution). The present results contribute to understanding of the role of $Al(OH)_4^-$ in the activated waste glass system. The following detailed conclusions can be drawn:

- Sodium aluminate activator provides more $Al(OH)_4^-$ in the pore solution, which promotes the formation of C(N)−A−S−H gels (major product) and zeolite A (secondary product). Sodium hydroxides activated glass produces Si-high, Al- and Ca-low gel as the dominant reaction product.

- Along the curing, the gradually dissolved Ca^{2+} ions from slag form more Ca-rich rather than Na-rich C(N)−A−S−H gels regardless of activator types. Compared to Na^{+}, higher molecular weight and positive charges in Ca^{2+} are easier to be incorporated into C(N)−A−S−H gels. It also results in the shorter MCL of C(N)−A−S−H gels.
- Sodium aluminate provides more $Al(OH)_4^-$ in the relatively low pH environment in activated glass system. Aluminate tetrahedra acts as cross-linking agents, linking the silicate tetrahedra together and promoting the formation of a three-dimensional gel network. A longer MCL leads to more hydrogen sites (at end-chain Q^1 silicate specie), which can be replaced by cations on the silicate chain. More Na^{+} can be captured into the gels, forming more C(N)−A−S−H.
- The resistance of efflorescence is enhanced by the extra $Al(OH)_4^-$ from sodium aluminate activator that captures more Na^{+} to form Na-rich C(N)−A−S−H gels. Relatively low pH of sodium aluminate also lessens the risk of efflorescence of the matrix. Moreover, the sodium aluminate improves the mechanical property by supplementing extra Al resources to form a denser microstructure.

Nevertheless, shrinkages of the sodium aluminate activated waste glass and slag are observed, partially also due to the thermal curing process. Exploring approaches to deal with the shrinkage issue would be of scientific and practical interest in terms of sodium aluminate activated waste glass.

CRediT authorship contribution statement

Tao Liu: Data curation, Formal analysis, Investigation, Methodology, Resources, Writing – original draft. **Yuxuan Chen:** Investigation. **Bo Yuan:** Investigation. **Weitan Zhuang:** Investigation. **H.J.H. Brouwers:** Supervision, Funding acquisition. **Qingliang Yu:** Writing – review & editing, Supervision, Resources, Project administration, Investigation, Funding acquisition, Conceptualization.

Declaration of competing interest

The authors declare that they have no known competing financial interests or personal relationships that could have appeared to influence the work reported in this paper.

Data availability

Data will be made available on request.

Acknowledgment

This study is supported by Technical University of Denmark, Eindhoven University of Technology, and Wuhan University. Special thanks are expressed to Professor John L. Provis (Paul Scherrer Institute) for the fruitful discussions regarding the NMR analyses.

Appendix A

Table A1
Quantification of XRD results at 3 days (wt%).

	NA3–3d	NA4-3d	NA5-3d	NHNA3–3d	NHNA4-3d	NHNA5-3d	NH3–3d	NH4-3d	NH5-3d
Calcite	0.00	0.00	0.00	1.00	1.30	1.53	1.04	1.59	1.38
Hydrotalcite	0.00	0.00	0.00	0.00	0.00	0.00	0.51	0.92	0.66
Katoite	0.00	1.68	1.97	0.88	0.63	0.43	0.00	0.00	0.00
Zeolite Na-P_1	0.00	0.03	0.07	1.12	10.69	16.07	0.00	0.00	0.00
Natrite	0.00	0.61	0.29	0.80	0.49	0.86	2.33	4.39	6.01
Zeolite A	3.04	3.20	3.27	3.56	0.76	0.34	0.00	0.00	0.00
Amor.	96.96	94.47	94.40	92.63	86.12	80.77	96.11	93.10	91.96

Table A2
Quantification of XRD results at 28 days (wt. %).

	NA3–3d	NA4-3d	NA5-3d	NHNA3–3d	NHNA4-3d	NHNA5-3d	NH3–3d	NH4-3d	NH5-3d
Calcite	0.00	0.00	0.00	0.88	2.21	1.93	1.00	1.52	1.94
Hydrotalcite	0.00	0.00	0.00	0.00	0.00	0.00	0.76	0.97	1.34
Katoite	0.00	4.83	6.18	0.48	0.76	0.24	0.00	0.00	0.00
Magnesite	0.00	0.00	0.00	1.51	2.41	1.54	1.66	2.67	3.11
Zeolite Na-P_1	0.00	2.50	0.80	1.11	17.16	20.40	0.00	0.00	0.00
Natrite	0.00	0.00	0.00	0.93	0.92	1.20	0.93	1.58	3.99
Zeolite A	5.34	8.19	8.36	2.79	0.93	0.60	0.00	0.00	0.00
Amor.	94.66	84.49	84.68	92.31	75.61	74.09	95.67	93.28	89.61

NA3

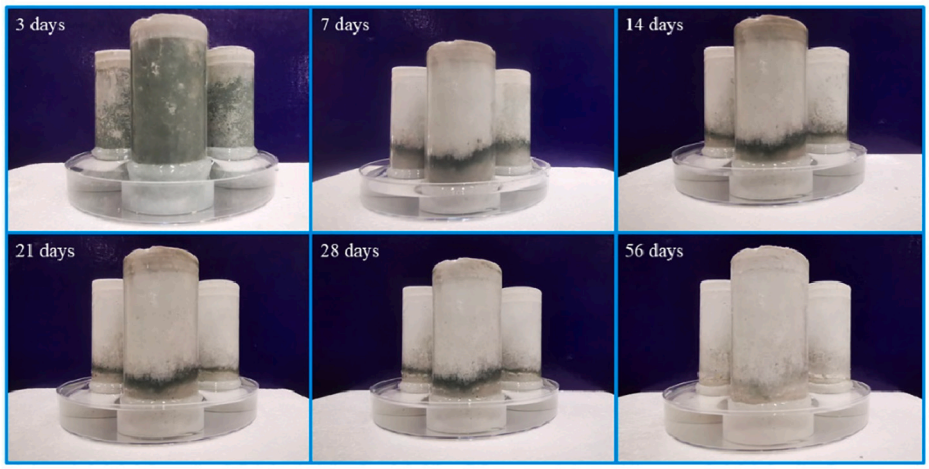

NA4

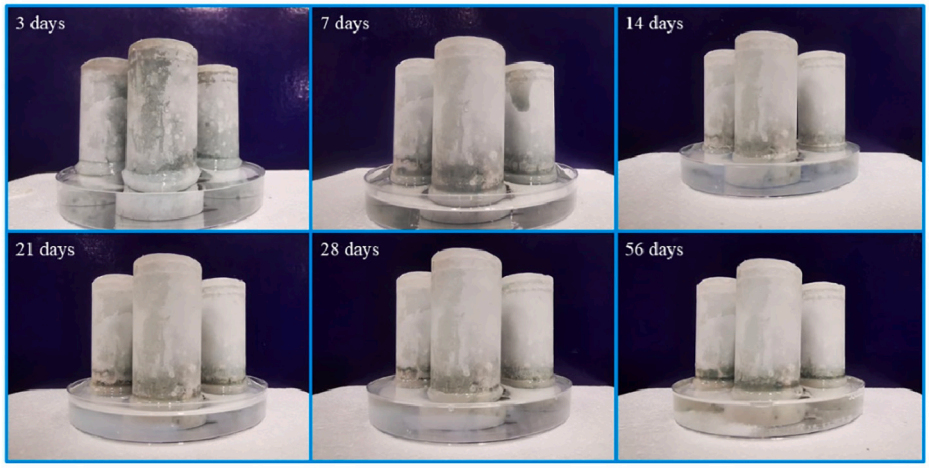

NA5

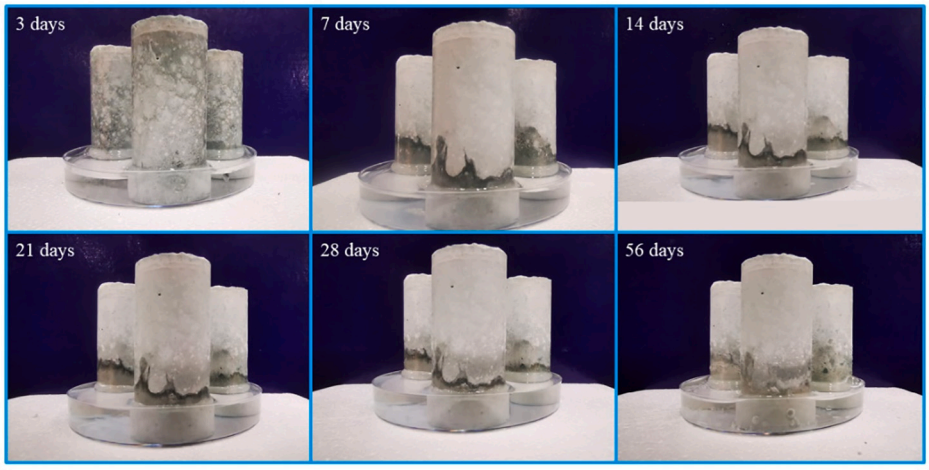

Fig. A1. Visual efflorescence testing of SAASG pastes at different curing ages.

NHNA3

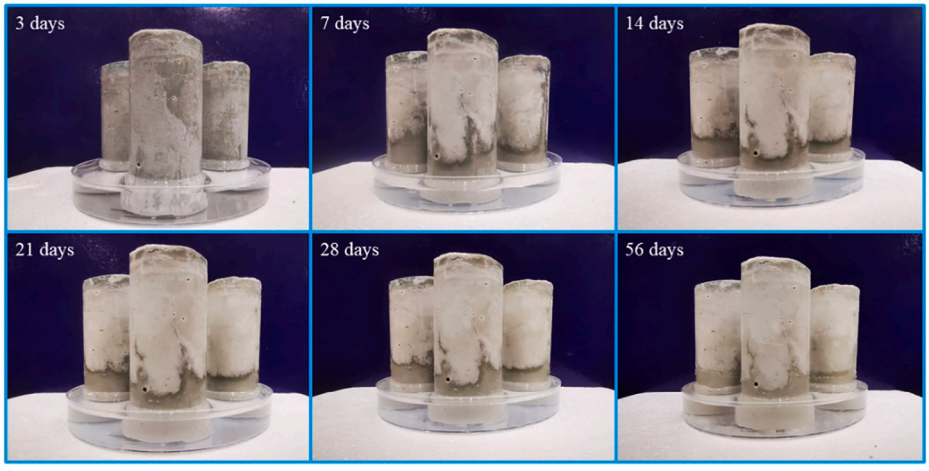

NHNA4

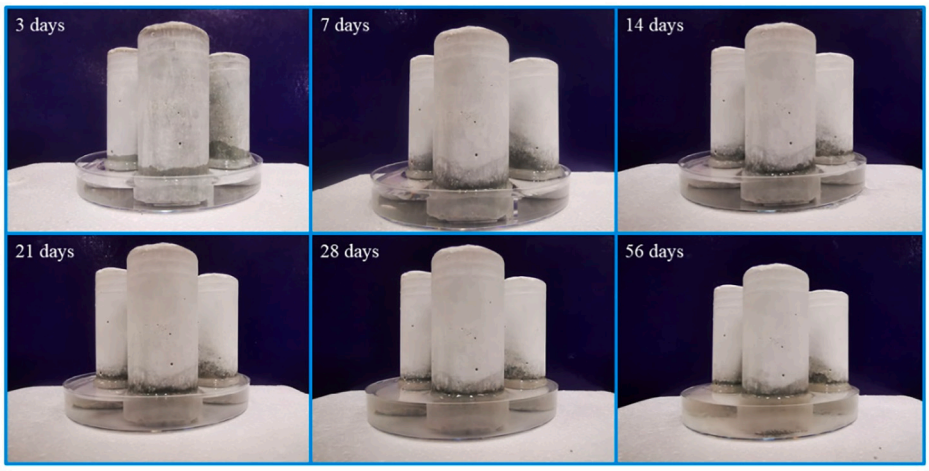

NHNA5

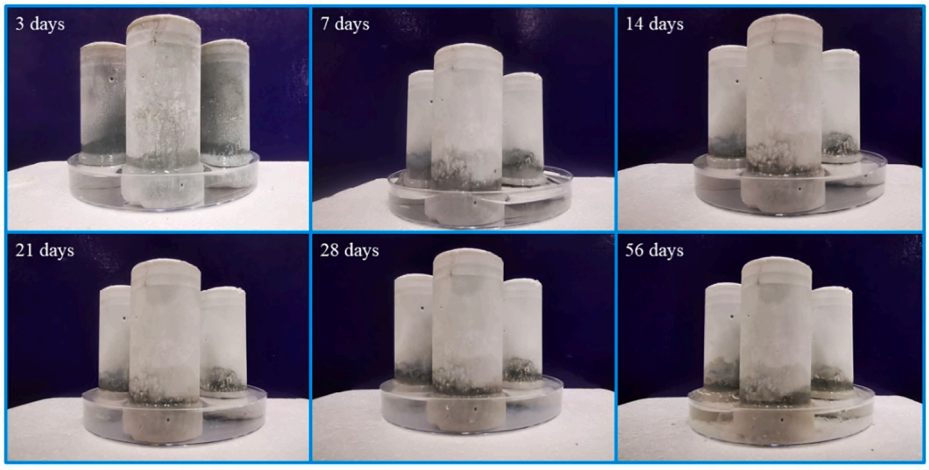

Fig. A1. (*continued*).

NH3

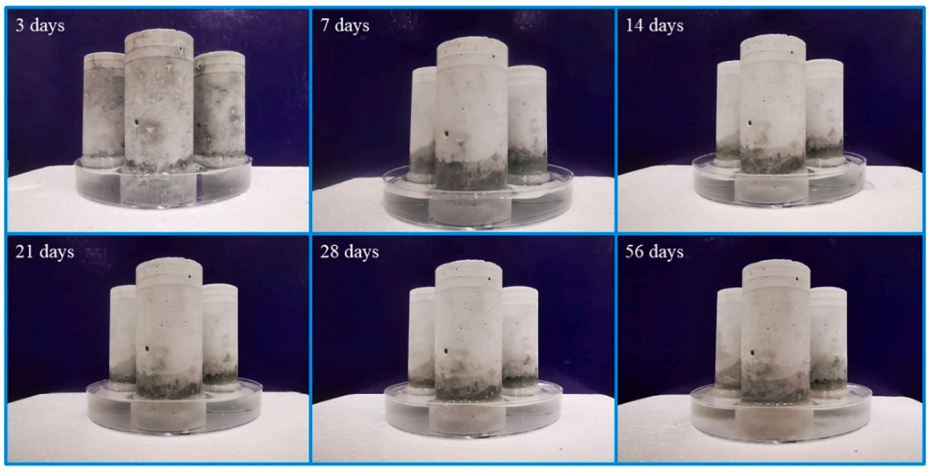

NH4

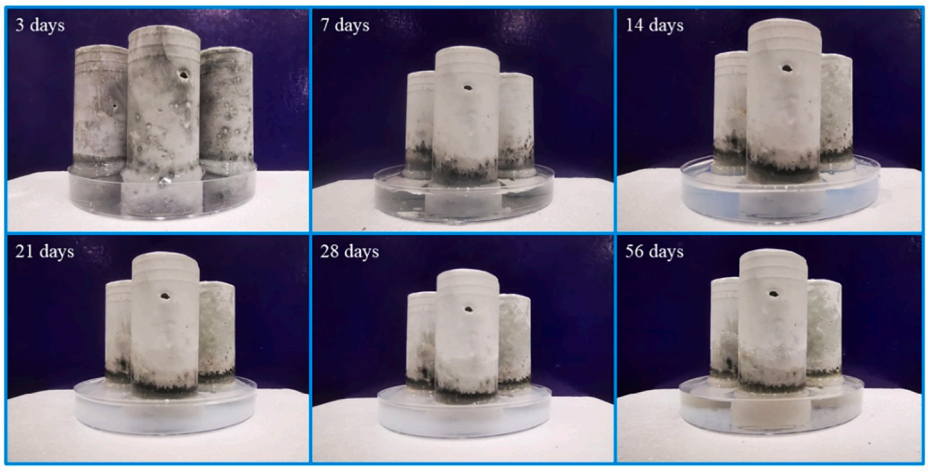

NH5

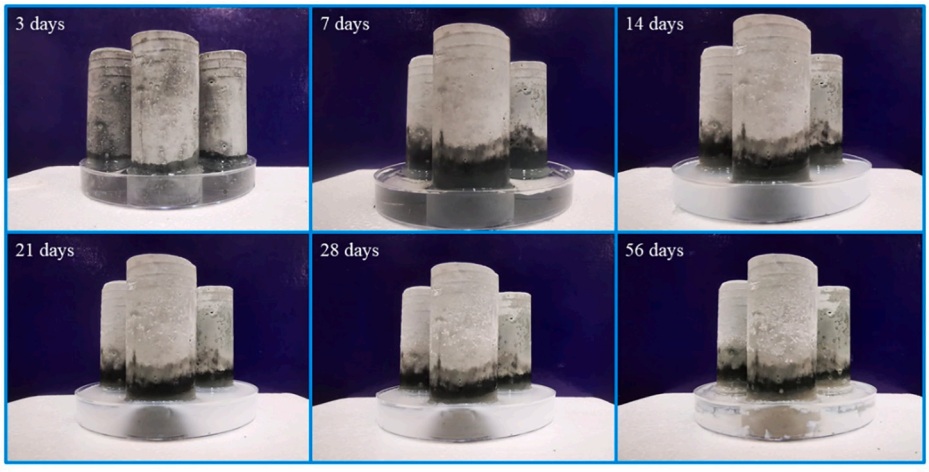

Fig. A1. (*continued*).

Appendix B. Supplementary data

Supplementary data to this article can be found online at https://doi.org/10.1016/j.cemconres.2024.107527.

References

[1] T.C. Ling, C.S. Poon, Spent fluorescent lamp glass as a substitute for fine aggregate in cement mortar, J. Clean. Prod. 161 (2017) 646–654, https://doi.org/10.1016/j.jclepro.2017.05.173.

[2] T. Liu, Q. Yu, H.J.H. Brouwers, X. Fan, Utilization of waste glass in alkali activated slag/fly ash blends: reaction process, microstructure, and chloride diffusion behavior, J. Sustain. Cem. Based Mater. 12 (2023) 516–526, https://doi.org/10.1080/21650373.2022.2082577.

[3] W.C. Wang, B.T. Chen, H.Y. Wang, H.C. Chou, A study of the engineering properties of alkali-activated waste glass material (AAWGM), Constr. Build. Mater. 112 (2016) 962–969, https://doi.org/10.1016/j.conbuildmat.2016.03.022.

[4] C.C. Wang, H.Y. Wang, B.T. Chen, Y.C. Peng, Study on the engineering properties and prediction models of an alkali-activated mortar material containing recycled waste glass, Constr. Build. Mater. 132 (2017) 130–141, https://doi.org/10.1016/j.conbuildmat.2016.11.103.

[5] M. Mastali, Z. Abdollahnejad, F. Pacheco-Torgal, Performance of waste based alkaline mortars submitted to accelerated carbon dioxide curing, Resour. Conserv. Recycl. 129 (2018) 12–19, https://doi.org/10.1016/j.resconrec.2017.10.017.

[6] R. Martinez-Lopez, J. Ivan Escalante-Garcia, Alkali activated composite binders of waste silica soda lime glass and blast furnace slag: strength as a function of the composition, Constr. Build. Mater. 119 (2016) 119–129, https://doi.org/10.1016/j.conbuildmat.2016.05.064.

[7] M. Torres-Carrasco, F. Puertas, Waste glass as a precursor in alkaline activation: chemical process and hydration products, Constr. Build. Mater. 139 (2017) 342–354, https://doi.org/10.1016/j.conbuildmat.2017.02.071.

[8] G. Liang, H. Li, H. Zhu, T. Liu, Q. Chen, H. Guo, Reuse of waste glass powder in alkali-activated metakaolin/fly ash pastes: physical properties, reaction kinetics and microstructure, Resour. Conserv. Recycl. 173 (2021), https://doi.org/10.1016/j.resconrec.2021.105721.

[9] R. Xiao, Y. Ma, X. Jiang, M. Zhang, Y. Zhang, Y. Wang, B. Huang, Q. He, Strength, microstructure, efflorescence behavior and environmental impacts of waste glass geopolymers cured at ambient temperature, J. Clean. Prod. 252 (2020), https://doi.org/10.1016/j.jclepro.2019.119610.

[10] Wenkui Dong Wenkui, L. Wengui, Professor Zhong Tao, A comprehensive review on performance of cementitious and geopolymeric concretes with recycled waste glass as powder, sand or cullet, Resour. Conserv. Recycl. 172 (2021).

[11] E. Najafi Kani, A. Allahverdi, J.L. Provis, Efflorescence control in geopolymer binders based on natural pozzolan, Cem. Concr. Compos. 34 (2012) 25–33, https://doi.org/10.1016/j.cemconcomp.2011.07.007.

[12] Y. Ge, X. Tian, D. Huang, Q. Zhong, Y. Yang, H. Peng, Understanding efflorescence behavior and compressive strength evolution of metakaolin-based geopolymer under a pore structure perspective, J. Build. Eng. 66 (2023), https://doi.org/10.1016/j.jobe.2023.105828.

[13] M.Z.Y. Ting, K.S. Wong, M.E. Rahman, S.J. Meheron, Deterioration of marine concrete exposed to wetting-drying action, J. Clean. Prod. 278 (2021), https://doi.org/10.1016/j.jclepro.2020.123383.

[14] H. Brocken, T.G. Nijland, White efflorescence on brick masonry and concrete masonry blocks, with special emphasis on sulfate efflorescence on concrete blocks, Constr. Build. Mater. 18 (2004) 315–323, https://doi.org/10.1016/j.conbuildmat.2004.02.004.

[15] M. Cyr, R. Idir, T. Poinot, Properties of inorganic polymer (geopolymer) mortars made of glass cullet, J. Mater. Sci. 47 (2012) 2782–2797, https://doi.org/10.1007/s10853-011-6107-2.

[16] R. Redden, N. Neithalath, Microstructure, strength, and moisture stability of alkali activated glass powder-based binders, Cem. Concr. Compos. 45 (2014) 46–56, https://doi.org/10.1016/j.cemconcomp.2013.09.011.

[17] M. Vafaei, A. Allahverdi, High strength geopolymer binder based on waste-glass powder, Adv. Powder Technol. 28 (2017) 215–222, https://doi.org/10.1016/j.apt.2016.09.034.

[18] M. Criado, A. Palomo, A. Fernández-Jiménez, Alkali activation of fly ashes. Part 1: effect of curing conditions on the carbonation of the reaction products, Fuel 84 (2005) 2048–2054, https://doi.org/10.1016/j.fuel.2005.03.030.

[19] A. Fernández-Jiménez, A. Palomo, I. Sobrados, J. Sanz, The role played by the reactive alumina content in the alkaline activation of fly ashes, Microporous Mesoporous Mater. 91 (2006) 111–119, https://doi.org/10.1016/j.micromeso.2005.11.015.

[20] I.G. Richardson, Tobermorite/jennite- and tobermorite/calcium hydroxide-based models for the structure of C-S-H: applicability to hardened pastes of tricalcium silicate, β-dicalcium silicate, Portland cement, and blends of Portland cement with blast-furnace slag, metakaol, Cem. Concr. Res. 34 (2004) 1733–1777, https://doi.org/10.1016/j.cemconres.2004.05.034.

[21] T. Liu, Q. Yu, H.J.H. Brouwers, In-situ formation of layered double hydroxides (LDHs) in sodium aluminate activated slag: the role of Al-O tetrahedra, Cem. Concr. Res. 153 (2022), https://doi.org/10.1016/j.cemconres.2021.106697.

[22] T. Liu, S. Li, Y. Chen, H.J.H. Brouwers, Q. Yu, In-situ formation of layered double hydroxides in MgO–NaAlO2-activated GGBS/MSWI BA: impact of Mg2+ on reaction mechanism and leaching behavior, Cem. Concr. Compos. 140 (2023) 105114, https://doi.org/10.1016/j.cemconcomp.2023.105114.

[23] T. Liu, In-Situ Formation of Layered Double Hydroxides (LDHs) in Alkali Activated Materials (AAMs), Eindhoven University of Technology, 2023.

[24] Y. Yan, B. Ma, G.D. Miron, D.A. Kulik, K. Scrivener, B. Lothenbach, Al uptake in calcium silicate hydrate and the effect of alkali hydroxide, Cem. Concr. Res. 162 (2022) 106957, https://doi.org/10.1016/j.cemconres.2022.106957.

[25] A. Mendes, W.P. Gates, J.G. Sanjayan, F. Collins, NMR, XRD, IR and synchrotron NEXAFS spectroscopic studies of OPC and OPC/slag cement paste hydrates, Mater. Struct./Materiaux et Constructions 44 (2011) 1773–1791, https://doi.org/10.1617/s11527-011-9737-6.

[26] Y.X. Chen, S. Li, B. Mezari, E.J.M. Hensen, R. Yu, K. Schollbach, H.J.H. Brouwers, Q. Yu, Effect of highly dispersed colloidal olivine nano-silica on early age properties of ultra-high performance concrete, Cem. Concr. Compos. 131 (2022), https://doi.org/10.1016/j.cemconcomp.2022.104564.

[27] B. Walkley, J.L. Provis, Solid-state nuclear magnetic resonance spectroscopy of cements, Mater. Today Adv. 1 (2019), https://doi.org/10.1016/j.mtadv.2019.100007.

[28] J. Skibsted, M.D. Andersen, The effect of alkali ions on the incorporation of aluminum in the calcium silicate hydrate (C-S-H) phase resulting from Portland cement hydration studied by 29Si MAS NMR, J. Am. Ceram. Soc. 96 (2013) 651–656, https://doi.org/10.1111/jace.12024.

[29] M. Daugaard Andersen, H.J. Jakobsen, J. Skibsted, Incorporation of aluminum in the calcium silicate hydrate (C-S-H) of hydrated Portland cements: a high-field 27Al and 29Si MAS NMR investigation, Inorg. Chem. 42 (2003) 2280–2287, https://doi.org/10.1021/ic020607b.

[30] G.W. Groves, I.G. Richardson, The structure of the calcium silicate hydrate phases present in hardened pastes of white Portland cement/blast-furnace slag blends, J. Mater. Sci. 32 (1997) 4793–4802.

[31] I.G. Richardson, A.R. Brough, G.W. Groves, C.M. Dobson, The characterization of hardened alkali-activated blast-furnace slag pastes and the nature of the calcium silicate hydrate (C-S-H) phase, Cem. Concr. Res. 24 (1994) 813–829, https://doi.org/10.1016/0008-8846(94)90002-7.

[32] M. Sayehi, G. Delahay, H. Tounsi, Synthesis and characterization of ecofriendly materials zeolite from waste glass and aluminum scraps using the hydrothermal technique, J. Environ. Chem. Eng. 10 (2022) 108561, https://doi.org/10.1016/j.jece.2022.108561.

[33] C.S. Cundy, P.A. Cox, The hydrothermal synthesis of zeolites: precursors, intermediates and reaction mechanism, Microporous Mesoporous Mater. 82 (2005) 1–78, https://doi.org/10.1016/j.micromeso.2005.02.016.

[34] B. Ma, B. Lothenbach, Synthesis, characterization, and thermodynamic study of selected Na-based zeolites, Cem. Concr. Res. 135 (2020) 106111, https://doi.org/10.1016/j.cemconres.2020.106111.

[35] T. Williamson, T. Zhu, J. Han, G. Sant, O.B. Isgor, M.C.G. Juenger, L. Katz, Effect of temperature on N-A-S-(H) and zeolite composition, solubility, and structure, Cem. Concr. Res. 172 (2023) 107213, https://doi.org/10.1016/j.cemconres.2023.107213.

[36] M. Jin, Y. Ma, W. Li, J. Huang, Y. Yan, H. Zeng, C. Lu, J. Liu, Multi-scale investigation on composition-structure of C-(a)-S-H with different Al/Si ratios under attack of decalcification action, Cem. Concr. Res. 172 (2023) 107251, https://doi.org/10.1016/j.cemconres.2023.107251.

[37] N.M. Musyoka, L.F. Petrik, E. Hums, A. Kuhnt, W. Schwieger, Thermal stability studies of zeolites a and X synthesized from south African coal fly ash, Res. Chem. Intermed. 41 (2015) 575–582, https://doi.org/10.1007/s11164-013-1211-3.

[38] M.M. Kumar, H. Jena, Direct single-step synthesis of phase pure zeolite Na–P1, hydroxy sodalite and analcime from coal fly ash and assessment of their Cs+ and Sr2+ removal efficiencies, Microporous Mesoporous Mater. 333 (2022), https://doi.org/10.1016/j.micromeso.2022.111738.

[39] A. Jiménez, V. Rives, M.A. Vicente, Thermal study of the hydrocalumite–katoite–calcite system, Thermochim. Acta 713 (2022) 179242, https://doi.org/10.1016/j.tca.2022.179242.

[40] J.W. Kim, H.G. Lee, Thermal and carbothermic decomposition of Na2CO3 and Li2CO3, Metall. Mater. Trans. B Process Metall. Mater. Process. Sci. 32 (2001) 17–24, https://doi.org/10.1007/s11663-001-0003-0.

[41] C. Forano, U. Costantino, V. Prévot, C.T. Gueho, Layered double hydroxides (LDH), Dev. Clay Sci. 5 (2013) 745–782, https://doi.org/10.1016/B978-0-08-098258-8.00025-0.

[42] T. Liu, Y. Chen, Q. Yu, J. Fan, H.J.H. Brouwers, Effect of MgO, mg-Al-NO3 LDH and calcined LDH-CO3 on chloride resistance of alkali activated fly ash and slag blends, Constr. Build. Mater. 250 (2020), https://doi.org/10.1016/j.conbuildmat.2020.118865.

[43] S. Dadsetan, H. Siad, M. Lachemi, O. Mahmoodi, M. Sahmaran, Optimization and characterization of geopolymer binders from ceramic waste, glass waste and sodium glass liquid, J. Clean. Prod. 342 (2022), https://doi.org/10.1016/j.jclepro.2022.130931.

[44] W. Mozgawa, M. Król, J. Dyczek, J. Deja, Investigation of the coal fly ashes using IR spectroscopy, Spectrochim. Acta A Mol. Biomol. Spectrosc. 132 (2014) 889–894, https://doi.org/10.1016/j.saa.2014.05.052.

[45] B. Walkley, R. San Nicolas, M.A. Sani, G.J. Rees, J.V. Hanna, J.S.J. van Deventer, J. L. Provis, Phase evolution of C-(N)-A-S-H/N-A-S-H gel blends investigated via alkali-activation of synthetic calcium aluminosilicate precursors, Cem. Concr. Res. 89 (2016) 120–135, https://doi.org/10.1016/j.cemconres.2016.08.010.

[46] G. Bin Cai, S.F. Chen, L. Liu, J. Jiang, H. Bin Yao, A.W. Xu, S.H. Yu, 1,3-Diamino-2-hydroxypropane-N,N,N′,N′-tetraacetic acid stabilized amorphous calcium carbonate: Nucleation, transformation and crystal growth, CrystEngComm 12 (2010) 234–241. doi:https://doi.org/10.1039/b911426m.

[47] W. Mozgawa, W. Jastrzębski, M. Handke, Vibrational spectra of D4R and D6R structural units, J. Mol. Struct. 744–747 (2005) 663–670, https://doi.org/10.1016/j.molstruc.2004.12.051.

[48] Y. Zhan, X. Li, Y. Zhang, L. Han, Y. Chen, Phase and morphology control of LTA/FAU zeolites by adding trace amounts of inorganic ions, Ceram. Int. 39 (2013) 5997–6003, https://doi.org/10.1016/j.ceramint.2013.01.005.

[49] M. Sayehi, G. Garbarino, G. Delahay, G. Busca, H. Tounsi, Synthesis of high value-added Na–P1 and Na-FAU zeolites using waste glass from fluorescent tubes and

aluminum scraps, Mater. Chem. Phys. 248 (2020), https://doi.org/10.1016/j.matchemphys.2020.122903.
[50] Durability of alkali-activated materials with different C–S–H and N-A-S-H gels in acid and alkaline environment, (n.d.).
[51] S. Zhang, Z. Li, B. Ghiassi, S. Yin, G. Ye, Fracture properties and microstructure formation of hardened alkali-activated slag/fly ash pastes, Cem. Concr. Res. 144 (2021) 106447, https://doi.org/10.1016/j.cemconres.2021.106447.
[52] N.V. Chukanov, Infrared spectra of mineral species: extended library, infrared spectra of mineral species: extended, Library 1 (2014) 21–1701.
[53] P.J. Schilling, L.G. Butler, A. Roy, H.C. Eaton, 29Si and 27Al MAS-NMR of NaOH-activated blast-furnace slag, J. Am. Ceram. Soc. 77 (1994) 2363–2368, https://doi.org/10.1111/j.1151-2916.1994.tb04606.x.
[54] B. Walkley, X. Ke, J.L. Provis, S.A. Bernal, Activator anion influences the nanostructure of alkali-activated slag cements, J. Phys. Chem. C 125 (2021) 20727–20739, https://doi.org/10.1021/acs.jpcc.1c07328.
[55] F. Souayfan, E. Rozière, M. Paris, D. Deneele, A. Loukili, C. Justino, 29Si and 27Al MAS NMR spectroscopic studies of activated metakaolin-slag mixtures, Constr. Build. Mater. 322 (2022), https://doi.org/10.1016/j.conbuildmat.2022.126415.
[56] L.E. Menchaca-Ballinas, A.V. Gorokhovsky, J.I. Escalante-Garcia, Waste glass as a precursor in sustainable hydraulic cements activated with CaO-NaOH-Na2CO3, Constr. Build. Mater. 302 (2021), https://doi.org/10.1016/j.conbuildmat.2021.124099.
[57] F. Puertas, M. Torres-Carrasco, Use of glass waste as an activator in the preparation of alkali-activated slag, Mechanical strength and paste characterisation, Cem. Concr. Res. 57 (2014) 95–104, https://doi.org/10.1016/j.cemconres.2013.12.005.
[58] J. Davidovits, Geopolymer Chemistry and Applications, 5-th edition, J, Davidovits.–Saint-Quentin, France, 2020, p. 680.
[59] S.Y. Yang, Y. Yan, B. Lothenbach, J. Skibsted, Incorporation of sodium and aluminum in cementitious calcium-Alumino-silicate-hydrate C-(a)-S-H phases studied by 23Na, 27Al, and 29Si MAS NMR spectroscopy, J. Phys. Chem. C 125 (2021) 27975–27995, https://doi.org/10.1021/acs.jpcc.1c08419.
[60] B. Walkley, R. San Nicolas, M.A. Sani, G.J. Rees, J.V. Hanna, J.S.J. van Deventer, J. L. Provis, Phase evolution of C-(N)-A-S-H/N-A-S-H gel blends investigated via alkali-activation of synthetic calcium aluminosilicate precursors, Cem. Concr. Res. 89 (2016) 120–135, https://doi.org/10.1016/j.cemconres.2016.08.010.
[61] Y. Chiang, S.W. Chang, Bridging the gap between NMR measured mean silicate chain length and nano-scale silicate polymorphism of calcium silicate hydrates, Cem. Concr. Res. 140 (2021), https://doi.org/10.1016/j.cemconres.2020.106268.
[62] S.A. Bernal, J.L. Provis, B. Walkley, R. San Nicolas, J.D. Gehman, D.G. Brice, A. R. Kilcullen, P. Duxson, J.S.J. Van Deventer, Gel nanostructure in alkali-activated binders based on slag and fly ash, and effects of accelerated carbonation, Cem. Concr. Res. 53 (2013) 127–144, https://doi.org/10.1016/j.cemconres.2013.06.007.
[63] J. Wang, Z. Hu, Y. Chen, J. Huang, Y. Ma, W. Zhu, J. Liu, Effect of ca/Si and Al/Si on micromechanical properties of C(−a)-S-H, Cem. Concr. Res. 157 (2022) 106811, https://doi.org/10.1016/j.cemconres.2022.106811.
[64] K. Shimoda, Y. Tobu, K. Kanehashi, T. Nemoto, K. Saito, Total understanding of the local structures of an amorphous slag: perspective from multi-nuclear (29Si, 27Al, 17O, 25Mg, and 43Ca) solid-state NMR, J. Non-Cryst. Solids 354 (2008) 1036–1043, https://doi.org/10.1016/j.jnoncrysol.2007.08.010.
[65] R.J. Myers, S.A. Bernal, J.D. Gehman, J.S.J. Van Deventer, J.L. Provis, The role of al in cross-linking of alkali-activated slag cements, J. Am. Ceram. Soc. 98 (2015) 996–1004, https://doi.org/10.1111/jace.13360.
[66] J.Z. Hu, C. Wan, A. Vjunov, M. Wang, Z. Zhao, M.Y. Hu, D.M. Camaioni, J. A. Lercher, 27Al MAS NMR studies of HBEA zeolite at low to high magnetic fields, J. Phys. Chem. C 121 (2017) 12849–12854, https://doi.org/10.1021/acs.jpcc.7b03517.
[67] X. Pardal, F. Brunet, T. Charpentier, I. Pochard, A. Nonat, 27Al and 29Si solid-state NMR characterization of calcium-aluminosilicate-hydrate, Inorg. Chem. 51 (2012) 1827–1836, https://doi.org/10.1021/ic202124x.
[68] K.L. Moran, P.D. Barker, J.E. Readman, P.P. Edwards, R. Dupree, P.A. Anderson, 29Si and 27Al MAS NMR spectra are affected by alkali metal cluster formation in zeolite LTA, Chem. Commun. (2000) 55–56, https://doi.org/10.1039/a908027i.
[69] S. Kalirai, P.P. Paalanen, J. Wang, F. Meirer, B.M. Weckhuysen, Visualizing Dealumination of a single zeolite domain in a real-life catalytic cracking particle, Ang. Chem. Int. Edit. 55 (2016) 11134–11138, https://doi.org/10.1002/anie.201605215.
[70] E. Pustovgar, R.K. Mishra, M. Palacios, J.B. d'Espinose de Lacaillerie, T. Matschei, A.S. Andreev, H. Heinz, R. Verel, R.J. Flatt, Influence of aluminates on the hydration kinetics of tricalcium silicate, Cem. Concr. Res. 100 (2017) 245–262, https://doi.org/10.1016/j.cemconres.2017.06.006.
[71] M.D. Andersen, H.J. Jakobsen, J. Skibsted, A new aluminium-hydrate species in hydrated Portland cements characterized by 27Al and 29Si MAS NMR spectroscopy, Cem. Concr. Res. 36 (2006) 3–17, https://doi.org/10.1016/j.cemconres.2005.04.010.
[72] J. Davidovits, Properties of Geopolymer cements, First International Conference on Alkaline Cements and Concretes (1994) 131–149.
[73] L. John, Provis, Geopolymers and Related Alkali-Activated Materials, Annu Rev Mater Res, Susan A. Bernal, 2014, pp. 299–327.
[74] E. Kapeluszna, Ł. Kotwica, A. Różycka, Ł. Gołek, Incorporation of Al in C-A-S-H gels with various ca/Si and Al/Si ratio: microstructural and structural characteristics with DTA/TG, XRD, FTIR and TEM analysis, Constr. Build. Mater. 155 (2017) 643–653, https://doi.org/10.1016/j.conbuildmat.2017.08.091.
[75] I.G. Richardson, Tobermorite/jennite- and tobermorite/calcium hydroxide-based models for the structure of C-S-H: applicability to hardened pastes of tricalcium silicate, β-dicalcium silicate, Portland cement, and blends of Portland cement with blast-furnace slag, metakaol, Cem. Concr. Res. 34 (2004) 1733–1777, https://doi.org/10.1016/j.cemconres.2004.05.034.
[76] H.F.W. Taylor, Hydrated calcium silicates. Part I. Compound formation at ordinary temperatures, American concrete institute, ACI special, Publication SP-249 (2008) 67–79.
[77] H.F.W. Taylor, Nanostructure of CSH: current status, Adv. Cem. Based Mater. 1 (1993) 38–46, https://doi.org/10.1016/1065-7355(93)90006-A.
[78] Z. Yang, N. Xue, L. Xu, L. Yu, L. Huang, K. Wu, Evaluation of the efflorescence resistance of calcium sulfoaluminate cement mortar: from indoor accelerated testing to outdoor exposure, J. Mater. Res. Technol. 22 (2023) 2447–2461, https://doi.org/10.1016/j.jmrt.2022.12.061.
[79] J.L. Provis, G.C. Lukey, J.S.J. van Deventer, Do Geopolymers actually contain Nanocrystalline zeolites? A Reexamination of Existing Results, Chemistry of Materials 17 (2005) 3075–3085, https://doi.org/10.1021/cm050230i.
[80] Y. Wang, Y. Cao, Z. Zhang, P. Zhang, Y. Ma, A. Wang, H. Wang, Intrinsic sulfuric acid resistance of C-(N)-A-S-H and N-A-S-H gels produced by alkali-activation of synthetic calcium aluminosilicate precursors, Cem. Concr. Res. 165 (2023) 107068, https://doi.org/10.1016/j.cemconres.2022.107068.
[81] R.R. Lloyd, J.L. Provis, J.S.J. Van Deventer, Pore solution composition and alkali diffusion in inorganic polymer cement, Cem. Concr. Res. 40 (2010) 1386–1392, https://doi.org/10.1016/j.cemconres.2010.04.008.
[82] L. Srinivasamurthy, V.S. Chevali, Z. Zhang, M.A. Longhi, T.W. Loh, H. Wang, Mechanical property and microstructure development in alkali activated fly ash slag blends due to efflorescence, Constr. Build. Mater. 332 (2022), https://doi.org/10.1016/j.conbuildmat.2022.127273.
[83] Z. Shi, C. Shi, S. Wan, N. Li, Z. Zhang, Effect of alkali dosage and silicate modulus on carbonation of alkali-activated slag mortars, Cem. Concr. Res. 113 (2018) 55–64, https://doi.org/10.1016/j.cemconres.2018.07.005.
[84] R.M. Novais, G. Ascensão, M.P. Seabra, J.A. Labrincha, Waste glass from end-of-life fluorescent lamps as raw material in geopolymers, Waste Manag. 52 (2016) 245–255, https://doi.org/10.1016/j.wasman.2016.04.003.